#### **OPEN ACCESS**



# Atomic Iron and Nickel in the Coma of C/1996 B2 (Hyakutake): Production Rates, Emission Mechanisms, and Possible Parents

S. J. Bromley 1 B. Neff<sup>2</sup>, S. D. Loch 1 J. P. Marler 2 J. Országh 3 K. Venkataramani 4 J. and D. Bodewits 1 Department of Physics, Auburn University, Leach Science Center, Auburn, AL 36832, USA; sjb0068@auburn.edu

2 Department of Physics and Astronomy, Clemson University, Clemson, SC 29630, USA

3 Department of Experimental Physics, Faculty of Mathematics, Physics and Informatics, Comenius University in Bratislava, Mlynská dolina F-2, 842 48 Bratislava;

Slovak Republic

Received 2021 June 8; revised 2021 September 27; accepted 2021 October 7; published 2021 November 16

#### Abstract

Two papers recently reported the detection of gaseous nickel and iron in the comae of over 20 comets from observations collected over two decades, including interstellar comet 2I/Borisov. To evaluate the state of the laboratory data in support of these identifications, we reanalyzed archived spectra of comet C/1996 B2 (Hyakutake), one of the nearest and brightest comets of the past century, using a combined experimental and computational approach. We developed a new, many-level fluorescence model that indicates that the fluorescence emissions of Fe I and Ni I vary greatly with heliocentric velocity. Combining this model with laboratory spectra of an Fe-Ni plasma, we identified 22 lines of Fe I and 14 lines of Ni I in the spectrum of Hyakutake. Using Haser models, we estimate the nickel and iron production rates as  $Q_{\rm Ni} = (2.6-4.1) \times 10^{22} \, {\rm s}^{-1}$  and  $Q_{\rm Fe} = (0.4-2.8) \times 10^{23} \, {\rm s}^{-1}$ . From derived column densities, the Ni/Fe abundance ratio  $\log_{10}[{\rm Ni/Fe}] = -0.15 \pm 0.07$  deviates significantly from solar abundance ratios, and it is consistent with the ratios observed in solar system comets. Possible production and emission mechanisms are analyzed in the context of existing laboratory measurements. Based on the observed spatial distributions, excellent fluorescence model agreement, and Ni/Fe ratio, our findings support an origin consisting of a short-lived unknown parent followed by fluorescence emission. Our models suggest that the strong heliocentric velocity dependence of the fluorescence efficiencies can provide a meaningful test of the physical process responsible for the Fe I and Ni I emission.

*Unified Astronomy Thesaurus concepts:* Laboratory astrophysics (2004); Comets (280); Atomic spectroscopy (2099); Spectral line identification (2073)

# 1. Introduction

Comets are the remnants of a protoplanetary disk, formed by accretion and preserved in the far reaches of our solar system. Upon transit toward the Sun, solar irradiation of the surface sublimates the ices, liberating gas and dust into an expanding cloud known as the coma. Whereas the properties of the nucleus cannot be sampled directly by remote observations, atoms and molecules in the coma enable the study of both the atomic and molecular vestiges of the early solar system. These molecules primarily consist of H, C, N, S, and O in various formulations (Altwegg et al. 2019). The bulk ices in the nucleus are H<sub>2</sub>O, CO, and CO<sub>2</sub>, mixed with other trace species, some of which may reside primarily in the dust (Rubin et al. 2019). Solar radiation photodissociates and photoionizes the molecules, leading to many radicals and atomic fragments (Feldman et al. 2004). Fragment species have many bright emission features in the visible and near-ultraviolet wavelengths, making them an easily accessible proxy to parent species (see A'Hearn et al. 1995).

Thus far, the molecular inventory of comets numbers in the dozens, ranging from  $\sim 30$  parent species visible from ground-based observations (Bockelée-Morvan & Biver 2017) and doubling to  $\sim 56$  total in situ (see 67P/Churyumov-Gerasimenko; Altwegg et al. 2019). The detection of molecules in

Original content from this work may be used under the terms of the Creative Commons Attribution 4.0 licence. Any further distribution of this work must maintain attribution to the author(s) and the title of the work, journal citation and DOI.

cometary comae sheds light on the abundances and trace organic chemistry during solar system formation.

Metal atoms, on the other hand, are mostly present in refractory materials. They have been discovered in, e.g., the sample return mission Stardust, which collected dust from comet 81P/Wild 2 and revealed the presence of, among others, copper (Cu), iron (Fe), nickel (Ni), and zirconium (Zr) contained in olivine, sulfides, and other mineral structures (Berger et al. 2011; Brownlee 2014). Ca, Fe, K, Li, and Na, which are normally absent in Jupiter's atmosphere, were detected after the impact of D/1993 F2 (Shoemaker-Levy 9; Roos-Serote et al. 1995). Neutral and ionized Mg and Fe were detected in UV spectroscopy through meteorites in Mars's atmosphere after the close encounter with C/2013 A1 (Siding Spring) in 2014 October (Crismani et al. 2018). Neutral sodium (Na I) has been detected in several comets, including the tail of comet C/1995 O1 (Hale-Bopp; Cremonese et al. 2002), C/ 1996 B2 (Hyakutake; Wyckoff et al. 1999), and most recently C/ 2020 F3 (NEOWISE). These detections summarize the limitations of detecting atomic metals in comets, where these endeavors often require extreme events such as close approaches or direct collisions that liberate atoms from within the bulk composition of the nucleus.

In the absence of extreme conditions, detections are even rarer, being limited to sungrazing comets that traverse close to the Sun (Jones et al. 2017). At 1 to several au, temperatures ( $<300~\rm K$ ) are insufficient for sublimating refractories or sulfides, which require  $T \ge 680~\rm K$  (Pollack et al. 1994). Sungrazers experience temperatures sufficient for sublimating metal-containing minerals such as olivine (Mg,Fe)<sub>2</sub>SiO<sub>4</sub> that are otherwise inert at the 1–3 au distances common to most

spectroscopic studies. The most famous sungrazer to date was comet C/1965 S1 (Ikeya-Seki), which passed the Sun as close as  $1.7\,R_\odot$  (0.008 au) in 1965. The analyses by Preston (1967) at  $13\,R_\odot$  and Slaughter (1969) at  ${\sim}30\,R_\odot$  revealed lines of Ca I, Ca II, Co I, Cu I, Fe I, K I, Mn I, Na I, Ni I, and V I, from which an effective excitation of 4480 K was derived, suggesting that metal atoms in the coma were excited by fluorescence. Thousands of sungrazers are known, but most are very small, are too faint, and/or approach the Sun too closely for spectroscopy (Jones et al. 2017).

Most recently, Manfroid et al. (2021) reported detections of (gaseous) Fe I and Ni I in the UV-visible range from a large sample of solar system comets observed with ESO's Very Large Telescope. Rather fortuitously, the available compilations of atomic data for Fe I and Ni I in the National Institute of Standards and Technology (NIST) Atomic Spectra Database (hereafter denoted ASD; Kramida et al. 2020) are considerable, allowing for development of a detailed many-level atomic fluorescence model. Assuming that the emission is driven by fluorescence, Manfroid et al. (2021) derived production rates and abundances of both iron and nickel from dozens of emission lines. While the production rates of these species are low (~g s<sup>-1</sup>), the large fluorescence efficiencies enabled their detection.

The molecular parents of these metal atoms are currently unknown. As proposed by Manfroid et al. (2021), one possibility is iron and nickel carbonyls, i.e., Fe(CO)<sub>5</sub> and Ni(CO)<sub>4</sub>, whose sublimation temperatures are comparable to that of CO (Manfroid et al. 2021), which would explain how metallic emission was observed even at large heliocentric distances up to 3.5 au. Interestingly, these detections are not limited to solar system objects; the interstellar object 2I/Borisov was recently observed by Guzik & Drahus (2021) at 2.3 au, revealing nine atomic Ni emission features in the same wavelength window as Manfroid et al. (2021). Taken together, it appears that the parents of both metals may be ubiquitous in cometary nuclei and suggest an as-yet-unexplored aspect of organic chemistry (see Klotz et al. 1996).

In this work, we present a new open-source model of the fluorescence emission of nickel and iron atoms based on atomic data in the ASD. We compare these models to laboratory data of Fe I and Ni I that were acquired as a background measurement for plasma experiments, and archived spectra of C/1996 B2 Hyakutake. These comparisons allowed us to confirm the line assignments of Manfroid et al. (2021) and Guzik & Drahus (2021), add to the inventory of metal lines present in regular cometary spectra, and to evaluate their excitation and formation mechanisms. The fluorescence model will be made publicly available to aid future observers.

The remainder of this work is as follows. In Section 2, the laboratory spectra of iron and nickel are discussed, and an overview of the archived spectra of C/1996 B2 (Hyakutake) is provided. In Section 3, the development of a fluorescence model utilizing the full extent of the available laboratory data is discussed. We detail the software implementation of our model, evaluate the propagation of the uncertainties of atomic data through to the fluorescence spectrum, and benchmark our model against spectra of C/1965 S1 (Ikeya-Seki). In Section 4, observed lines of Ni I and Fe I are discussed, with special attention on the validity of the identifications. Lastly, in

Section 5 we compare our production rates and Ni/Fe abundances to previous works and elaborate on complexities of the parent identification.

#### 2. Data

#### 2.1. Experimental Data

The laboratory spectra utilized here were collected during the measurement campaign of Au I and Au II emission reported in Bromley et al. (2020). These experiments used multiple probes containing stainless steel nickel-plated and gold-plated probes from which spectra of gold-iron-nickel plasmas and nickel-iron plasmas were collected. In short, the spectra were collected at resolving power  $\sim 5 \times 10^3$  between 200 and 800 nm from erosion of the probes inside the Compact Toroidal Hybrid plasma apparatus at Auburn University. A description of the apparatus and optical scheme is available in Hartwell et al. (2017) and Johnson et al. (2019). The spectra acquired in the lab lack emission from the "contaminants" OH, CO, CN, and other volatiles that emit within the 300-500 nm window of the comet spectra. However, the lab spectra also show features of H I and neutral and ionized C, N, and O. A detailed analysis of the Ni I and Ni II emission in the lab data will be reported in a future work (in preparation). Though the excitation mechanisms of our plasma experiment are obviously different compared to a comet (electron impact versus photofluorescence), the lab spectra confirm the positions and detections of Ni I emission lines. Electron-impact excitation also excites different levels than photofluorescence, allowing us to look for previously undocumented transitions (see Bodewits et al.2019).

# 2.2. Observations

The details of the observations, data reduction, and previous analyses of the C/1996 B2 (Hyakutake) spectra are discussed in Meier et al. (1998), Kim et al. (2003), A'Hearn et al. (2013), and A'Hearn et al. (2015a), and the data are available through NASA's Planetary Data System (A'Hearn et al. 2015b). In summary, the observations of comet C/1996 B2 (Hyakutake) were acquired on 1996 March 26 using the Echelle Spectrograph on the 4 m Mayall Telescope at Kitt Peak National Observatory. The comet was observed with a slit size of  $0.787 \times 7.4$ , where spectra were recorded in the range  $300-500 \,\mathrm{nm}$  with resolving power  $\sim 18,000$  (Meier et al. 1998). At the time of observation, the comet was traveling at  $-36.7 \,\mathrm{km \, s^{-1}}$  with respect to the Sun at a heliocentric distance of 1.02 au, and only 0.11 au from Earth. The spectra were wavelength and intensity calibrated using Th-Ar lamps at each echelon order (42 total). The archived spectra were corrected for the wavelength-dependent atmospheric extinction, and A'Hearn et al. (2015b) used spectra of solar analog 16 Cyg B and "sky flats" to remove the continuum caused by sunlight reflected by cometary dust. Wavelength calibrations are accurate to  $\pm 0.02\,\text{nm},$  and the (relative) intensity calibration within each order is estimated at the 5% level (Meier et al. 1998). However, overfilling of the slit during observations of solar analogs introduces an estimated  $\pm 40\%$  uncertainty on the absolute intensity calibration across the entire wavelength range.

<sup>&</sup>lt;sup>4</sup> Line list available as supplementary information at https://www.researchsquare.com/article/rs-101492/v1.

### 3. Fluorescence Model

While our laboratory spectra are useful for reporting line positions, the relative line heights cannot be directly compared to a comet spectrum, as the excitation mechanisms are fundamentally different. In a lab plasma, the spectrum varies as a function of the electron temperature and density. For fluorescing media, the spectrum is determined by the interplay of absorption, stimulated emission, and spontaneous emission, whose equilibrium balance will change with both heliocentric velocity and distance.

Using a fluorescence model, comparisons of synthetic versus observed spectra reveal clues on the physical process of atomic metal emission in the coma, as well as the chemical origins of these atoms. For example, fluorescence is unlikely to populate highly excited states, which are more likely to be excited from prompt emission. While one could assume a two-level model to study individual lines driven by absorption from the ground state, atoms with complex electronic structures require a many-level model to properly account for cascades and excited states populated by multiple absorption pathways.

We developed a fluorescence model assuming a collisionless and optically thin environment for the emitted photons, driven by three processes: (1) spontaneous emission, (2) stimulated emission, and (3) absorption. While the rate for (1) is a fundamental property, the rates for (2) and (3) derive from the rate of (1) and the local radiation field at the comet. In the following we outline our fluorescence model; the presentation of the matrices and differential equations is limited to two levels for readability.

Consider two levels of a many-level system with a transition from upper level j to lower level i. If the Einstein A-coefficient for (1),  $A_{j\rightarrow i}$ , is known, the coefficients for (2) and (3) may be expressed as

$$B_{j\to i} = \frac{\lambda_{ji}^5}{8\pi hc^2} A_{j\to i} \tag{1}$$

$$B_{i\to j} = \frac{g_j}{g} B_{j\to i},\tag{2}$$

where  $\lambda_{ji}$  is the (vacuum) wavelength of the transition,  $g_j = 2J_j + 1$ , and  $g_i = 2J_i + 1$ . For each B, the units [m<sup>3</sup> W<sup>-1</sup> s<sup>-1</sup>] ensure compatibility with the choice of solar spectrum described later. For a given pair of levels j and i, the change in population of the upper state j is written as

$$\frac{dn_{j}}{dt} = -A_{j\to i}n_{j} - B_{j\to i}n_{j} \int_{\lambda-\Delta\lambda}^{\lambda+\Delta\lambda} \phi(\lambda_{ij})\rho(\lambda_{ij})d\lambda 
+ B_{i\to j}n_{i} \int_{\lambda-\Delta\lambda}^{\lambda+\Delta\lambda} \phi(\lambda_{ij})\rho(\lambda_{ij})d\lambda,$$
(3)

where  $B_{ji}$  and  $B_{ij}$  are from Equations (1) and (2),  $\rho(\lambda)$  is the flux per wavelength interval (W m<sup>-3</sup>) incident on the population  $n_j$  at the energy of the transition from level j to level i, and  $\phi(\lambda_{ij})$  is the line shape (discussed in Section 3.1). The population of the lower state,  $n_i$ , may be written similarly as

$$\frac{dn_i}{dt} = A_{j\to i}n_j + B_{j\to i}n_j \int_{\lambda-\Delta\lambda}^{\lambda+\Delta\lambda} \phi(\lambda_{ij})\rho(\lambda_{ij})d\lambda 
- B_{i\to j}n_i \int_{\lambda-\Delta\lambda}^{\lambda+\Delta\lambda} \phi(\lambda_{ij})\rho(\lambda_{ij})d\lambda.$$
(4)

Abbreviating  $\sigma_{ij} \equiv \int_{\lambda - \Delta \lambda}^{\lambda + \Delta \lambda} \phi(\lambda_{ij}) \rho(\lambda_{ij}) d\lambda$ , the above system of equations for levels i and j may be written in matrix form as

$$\begin{bmatrix} -\sigma_{ij}B_{i\to j}A_{j\to i} + \sigma_{ij}B_{j\to i} \\ \sigma_{ij}B_{i\to j} - A_{j\to i} - \sigma_{ij}B_{j\to i} \end{bmatrix} \begin{bmatrix} n_i \\ n_j \end{bmatrix} = \begin{bmatrix} dn_i/dt \\ dn_j/dt \end{bmatrix}.$$
 (5)

In equilibrium, the populations are constant in time, and thus the right-hand side of Equation (5) is equal to 0. However, the matrix A is underdetermined, i.e., N equations and N-1 unknowns. We add an additional constraint by enforcing a normalization condition,  $\sum_i n_i = 1$ , by replacing all elements in row 0 of both the left and right matrices by 1. Our matrix equation thus takes the form

$$Ax = B, (6)$$

where the rates for processes (1)–(3) are stored in matrix A with populations contained within column vector x. For each pair of levels in the model, the transition rate contributes to two matrix elements: a positive contribution to the off-diagonal element (i,j), and a negative contribution to the diagonal element (j,j). Similarly, stimulated emission contributes positively to element (i,j) and negatively to element (j,j). Absorption provides a negative contribution to the diagonal term of level i at (i,i) and an off-diagonal, positive contribution to the population of  $n_j$  in element (j,i).

After populating matrices A and B, the equilibrium population fractions x follow as  $x = A^{-1} \times B$ . The transition intensity, i.e., the fluorescence efficiency ("g-factor") of the transition in units of J s<sup>-1</sup> particle<sup>-1</sup> at the emitting source from level j to level i, then follows from the level population  $n_i$  as

$$I_{j\to i} = \frac{hc}{\lambda_{ii}} n_j A_{j\to i},\tag{7}$$

where, given the directionality of stimulated emission along the Sun-comet vector, the contribution of stimulated emission to the observed line intensities is assumed to be negligible.

# 3.1. Computational Implementation

We implemented the fluorescence model in Section 3 in Python3. The code requires only standard Python packages and performs all mathematical operations using NumPy (Harris et al. 2020) and SciPy (Virtanen et al. 2020). SI units are utilized throughout, with conversions indicated where necessary. The code is made publicly available at the authors GitHub page.<sup>5</sup>

First, Einstein A-coefficients and level information (energies, J values) were retrieved from the NIST ASD (Kramida et al. 2020). From the level information, we generate wavelengths in vacuum ("Ritz" wavelengths) and convert to air wavelengths after all computations are carried out. For each transition, stimulated emission and absorption coefficients follow from Equations (1) and (2). To generate absorption and stimulated emission rates, we compiled a high-resolution solar spectrum from several space- and ground-based observations around solar minimum. Our (vacuum) flux atlas was therefore compiled as follows:

<sup>5</sup> https://github.com/StevenBromley/fluorescence\_model

- 1. Between 0 and 168 nm, we utilize the coronal/chromosphere far-ultraviolet solar model " $13 \times 1$ " of Fontenla et al. (2014).
- Between 168 and 200.06 nm, we assumed the solar spectrum collected during solar minimum from the SOLSTICE instrument with 0.1 nm resolution.<sup>6</sup>
- 3. For the small region between 200.06 and 202 nm, data from the Hall & Anderson (1991) data set were chosen to minimize discontinuities at the edges between adjacent data sets.
- 4. Between 202 and 2730 nm, we assumed the calibrated solar spectrum from Coddington et al. (2021), which itself was compiled from several high-resolution solar data sets, including the observations of Kurucz et al. (1984).

For each application the flux per wavelength interval  $\rho(\lambda)$  is rescaled to the comet's heliocentric distance by a factor of  $1/r_h^2$ . By default, our combined flux atlas is scaled to 1 au and will be made available in several forms (e.g., with/without the far-UV components) with our model code. The flux atlas is continuous at nearly all boundaries and integrates to 1327 W m<sup>-2</sup> at 1 au. The "missing" 3% flux, compared to a nominal integrated solar flux of  $\sim$ 1370 W m<sup>-2</sup>, arises from the infrared longward of 2730 nm. For wavelengths outside the bounds of the assumed solar spectrum, the code is capable of assuming a blackbody radiation field, defaulted to 5777 K.

If desired, the user is free to import and utilize any radiation field(s), such as those around stars other than the Sun for applications such as exocomet studies (Strøm et al. 2020) or handling fluorescence emission of Fe II in active galactic nuclei (Kovačević et al. 2010; Nierenberg et al. 2019). We note that our choice of solar spectrum is not applicable for solar conditions far from the conditions of solar minimum, particularly in the ultraviolet portion of the solar spectrum, which varies strongly with solar activity.

We tested the sensitivity of our model to the choice of solar spectrum by comparing fluorescence spectra generated using our compiled solar spectrum against those generated using the lower-resolution solar atlas spanning 200–1001 nm reported in Chance & Kurucz (2010). On average, *g*-factors calculated with this solar spectrum differ by ~10% for both Ni I and Fe I. In the range 300–400 nm, *g*-factors of Ni I are relatively insensitive at  $v_h = -36.7 \ \mathrm{km \ s^{-1}}$ , though some *g*-factors of Fe I show relative differences as high as 28%. The lower resolution of this solar spectrum (FWHM 0.5 nm vs. ~0.002 nm above) makes such a choice likely unsuitable for this application, and we use our compiled high-resolution solar spectrum for the remainder of this work.

When calculating the absorption and stimulated emission rates,  $W = B \int \phi(\lambda) \rho(\lambda) d\lambda$ , the Doppler shift of the solar spectrum resulting from the comet's heliocentric velocity (-36.7 km s<sup>-1</sup> during the archived observations of Hyakutake) is included by shifting the line center and line profile. For the line profile, two choices are provided: a delta function, and a Doppler (thermal) line profile. The Doppler profile width is taken as

$$\sigma_{\text{Doppler}} = \lambda_{ij} \sqrt{\frac{2k_b T}{mc^2}},$$
 (8)

Table 1
Einstein A-value Accuracy Scale in the NIST Atomic Spectra
Database (Kramida et al. 2020).

Flag	Uncertainty (%)	# Ni	# Fe
AAA	€0.3	0	0
AA	≤1	0	0
A+	€2	0	0
A	<b>≤</b> 3	0	149
B+	<b>≤</b> 7	0	282
В	≤10	0	622
C+	≤18	56	509
C	<b>≤</b> 25	126	205
D+	<b>≤</b> 40	45	188
D	<b>≤</b> 50	211	191
E	>50	84	393

Note. The number of lines with each rating for Ni I and Fe I are shown.

where c is the speed of light,  $k_b$  is the Boltzmann constant,  $T=279~r_h^{-1/2}$  (with  $r_h$  in AU) is the assumed blackbody temperature of the comet, and m is the mass of the emitting particle. For each line, the profile  $\phi(\lambda_{ij})$  is normalized such that  $\int \phi(\lambda) d\lambda = 1$  and is presented numerically on a (default) 500-point grid spanning  $\lambda_{ij} \pm 0.005$  nm. For models used to analyze the spectrum of C/1996 B2 (Hyakutake), Doppler line profiles with T=276 K are assumed.

After the initial matrix population, the inverse of the rate matrix  $(A^{-1})$  is calculated using the NumPy *linalg.inv* package, from which the populations follow as  $\mathbf{x} = A^{-1} \times B$ . For large singular or near-singular matrices caused by missing atomic data or small heliocentric distances (i.e., large absorption rates), the code attempts a solution using a pseudo-inverse (*linalg. pinv*) and/or singular value decomposition (*linalg.svd*). From the equilibrium populations, *g*-factors are calculated using Equation (7), and vacuum wavelengths are Doppler-shifted by the geocentric comet velocity before conversion to standard air wavelengths using the conversion of Morton (2000). We note that for the observation of C/1996 B2 (Hyakutake) utilized here the geocentric velocity was effectively  $0 \text{ km s}^{-1}$ , and the observation was recorded at  $\Delta = 0.11 \text{ au}$ .

Lastly, our model code directly imports the line and level lists that are downloaded from the ASD, and can thus be used to analyze any neutral or ionized atomic species for which the requisite data are available and all included levels are connected (directly or indirectly) to the ground state.

# 3.2. Error Propagation

The Einstein A-values were sourced from the ASD (Kramida et al. 2020), in which each A-value is assigned an accuracy rating. The ASD A-value accuracy scale is shown in Table 1 and spans from  $\leq 0.3\%$  to > 50%. Though some A-values used in our model may have large uncertainties in excess of 50%, line intensities from the model cannot simply be attributed an uncertainty equal to that of the A-value. For each transition, the six resulting contributions to the rate matrix each modify the detailed balance that determines the equilibrium populations. Therefore, we adopted the following Monte Carlo procedure for approximating the *uncorrelated* uncertainties of the model intensities from the A-value uncertainties.

Error bars on model intensities are derived by looking at changes in line intensities following the simultaneous

<sup>&</sup>lt;sup>6</sup> Available for download at https://lasp.colorado.edu/home/sorce/data/ssi-data/.

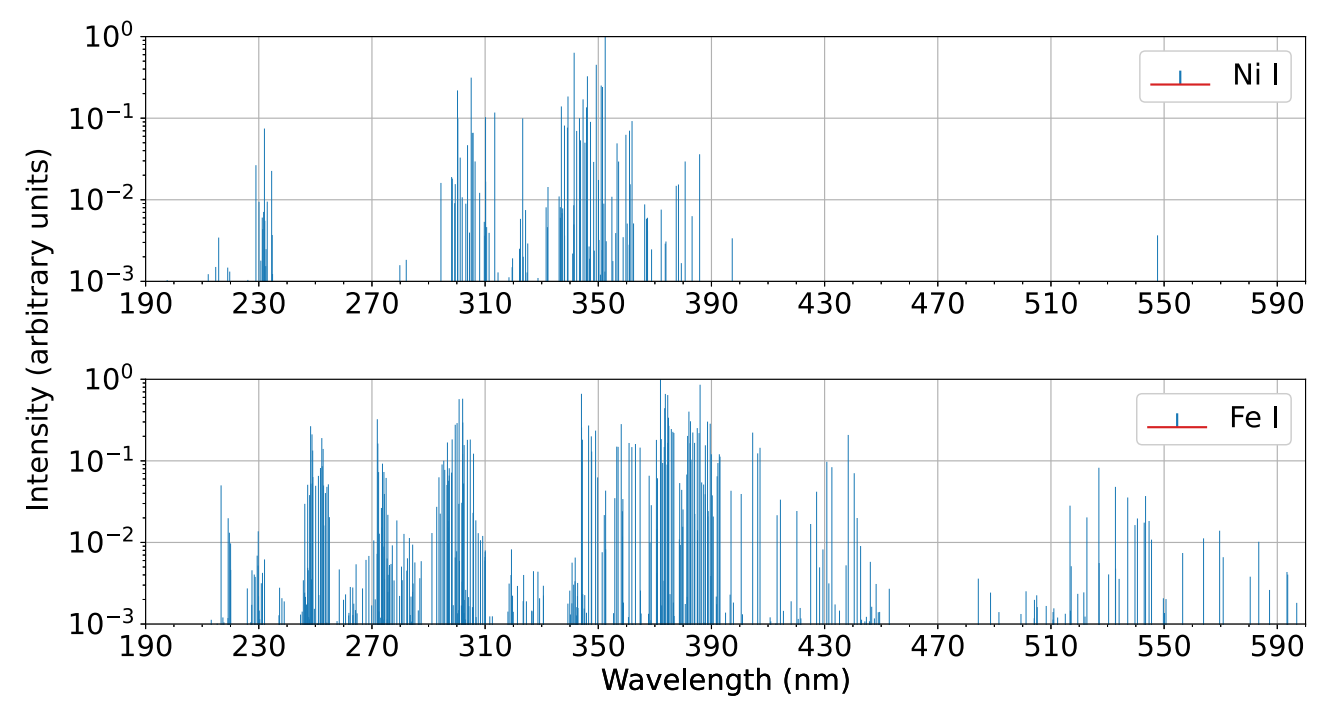


Figure 1. Synthetic fluorescence spectra stick plots on a logarithmic intensity scale with the strongest lines normalized to 1 for Ni I (top) and Fe I (bottom) spanning 190–600 nm. Line intensities were calculated for the observing conditions of C/1996 B2 Hyakutake,  $v_h = -36.7 \text{ km s}^{-1}$  and  $r_h = 1.02 \text{ au}$ .

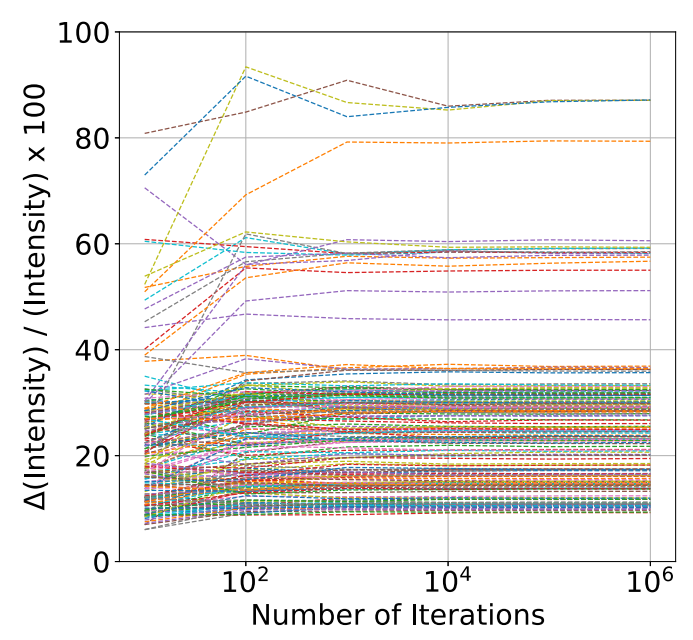
adjustment of all A-values. For each iteration, A-values are randomly and uniformly varied within a range of  $\pm$  the accuracy rating, e.g.,  $\pm$  10% for "B" ratings. For the lowest accuracy rating (E, >50%), we allow variations up to  $\pm$ 100%. We calculate the error bar for each emission line,  $\Delta I_{j\rightarrow i}$ , as the standard deviation of the line intensity across all iterations. We note that this is likely an overestimate of the uncorrelated uncertainty, as a Gaussian distribution (compared to the present uniformly distributed uncertainties) would favor lower variations for each A-value adjustment.

# 3.3. Ni I Model

For Ni I, the 522 transitions in the ASD were incorporated into our fluorescence model, involving 133 of the 288 known levels. For the 155 excluded levels, no transitions with transition rates were available. A synthetic spectrum of Ni I at 1.02 au and a heliocentric velocity  $v_h = -36.7 \text{ km s}^{-1}$  is shown in Figure 1 (top panel). The strongest emissions are between 300 and 390 nm. The model also suggests possibly observable emission (from space-based missions) around  $\sim$ 230 nm, but this emission is outside the bandpass of the archived spectrum of Hyakutake. The expected strongest emission overlaps with the wavelength ranges wherein nickel emission was identified by Manfroid et al. (2021) and Guzik & Drahus (2021).

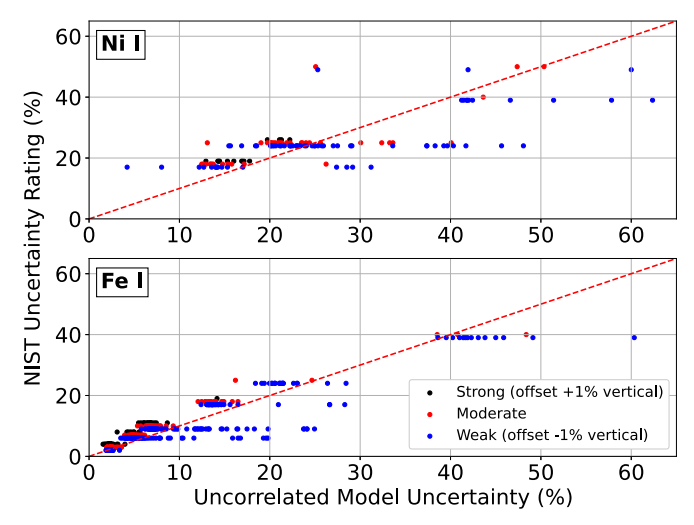
We derived error bars for the Ni I g-factors by iterating our Monte Carlo procedure with  $10^n$  (n=0-6) iterations at the observing conditions of C/1996 B2 (Hyakutake). Figure 2 shows the convergence of our method with increasing number of iterations; only lines in the range 300–500 nm are shown for visibility. The majority of the standard deviations converge by  $10^4$  iterations, which requires  $\sim 20$  minutes of compute time on a modern personal computer.

Figure 3 (top panel) shows the ratio of model standard deviation to model line intensity (in percentage) versus the



**Figure 2.** Ratio of line intensity standard deviation to line intensity (in percentage) for 213 Ni I lines spanning 300–500 nm as a function of iteration number (see text). Spectra were generated at the orbital conditions of the closest approach of C/1996 Hyakutake and are plotted at 10,  $10^2$ ,  $10^3$ ,  $10^4$ ,  $10^5$ , and  $10^6$  iterations. Each colored line shows the convergence of an individual transition.

NIST stated uncertainty rating (percentage) following  $10^6$  iterations for selected lines of Ni I. The dashed red line y=x is plotted as a visual aid only. "Strong" lines (black) are those with a model uncertainty with an intensity within a factor of 10 of the strongest line. "Moderate" lines (red) are those with  $10 < I_{\rm strongest}/I_{\rm line} < 100$ , and "weak" lines (blue) are those with  $100 < I_{\rm strongest}/I_{\rm line} < 1000$ . A total of 134 lines meeting these criteria are shown.



**Figure 3.** Top: model uncertainties for the fluorescence spectrum of Ni I, calculated as the standard deviation of line intensities following  $10^6$  iterations within the limits of  $\pm$  ASD accuracy (see Table 1) vs. the ASD accuracy rating for 134 selected transitions with model uncertainties <100%. Axis limits were restricted to enhance visibility of the majority (>99%) of lines within this criterion. Strong and weak lines are offset  $\pm1\%$  vertically with respect to moderate lines for visibility; for definitions of line classifications, see text. Bottom: Fe I model uncertainties vs. ASD accuracy ratings for 425 select transitions with uncertainties lower than 100%: 67 strong, 108 moderate, and 250 weak.

The remaining (not shown) lines are very weak and exhibit large model uncertainties. We note that the 84 "E"-rated lines all present significant sensitivity to our Monte Carlo procedure and exhibit extremely large uncertainties in excess of 10<sup>8</sup>%, owing to floating point errors and/or extremely small level populations. Thirty-nine of these 84 lines are E2 transitions between even-parity configurations where the upper levels are weakly populated by fluorescence; the dominant source of their population is absorption from the (already low) populations of excited odd-parity states. Twenty-one separate "E"-rated transitions are from excited even configurations to the excited odd configurations and suffer from a similar limitation. The remaining 24 "E"-rated transitions are outside our region of interest (300–500 nm).

For weak lines, the small scales of both level populations and fluorescence efficiencies present computational difficulties. For possible future investigations of particular lines using our model, it may be appropriate to investigate the model's sensitivity to changes in particular lines within some constraint, e.g., the effect of branching ratio uncertainty for a particular upper level. However, such an investigation is outside the scope of this work.

For strong and moderately strong lines, the model uncertainty is comparable to or less than the stated ASD uncertainty rating. The reason for this is likely due to the following: recall that for a two-level system the populations follow as

$$n_2 = n_1 \frac{W_{1 \to 2}}{W_{2 \to 1} + A_{2 \to 1}},\tag{9}$$

where  $W_{1\rightarrow 2}$  is the absorption rate,  $W_{2\rightarrow 1}$  is the stimulated emission rate, and  $A_{2\rightarrow 1}$  is the spontaneous emission rate. By definition, the Einstein *B*-coefficients are proportional to the *A*-value, and the net effect of an increase in *A*, e.g.,  $A\rightarrow 2\times A$ , propagates through the *B*-coefficients and leaves the ratio  $n_2/n_1$  unchanged. However, the change in *A*-value propagates

through the *g*-factor from Equation (7) as  $g_{2\rightarrow 1} \propto A_{2\rightarrow 1}$ , and thus the *g*-factor uncertainty is equal to the uncertainty of the transition rate.

For a many-level system, we find that intensities for levels that are well connected and well populated are less affected by changes in A-values compared to levels connected by fewer transitions, as the changes in multiple A-values partially cancel. For levels with one or few connections to the bulk of the levels, the uncertainty of the A-value more directly propagates through to the uncertainty of the line intensity. Given the scale of the Ni I rate matrix,  $133^2$  possible elements populated by  $522 \times 6 = 3132$  rates, the A-value iterations for well-populated levels (which thus produce the strongest lines) are effectively a perturbation. In this case, the quantity of atomic data, assumed to accurately reflect the totality of the level structure, including all important transitions, acts as a buffer against large fluctuations in model outputs for the strongest lines.

### 3.4. Fe I Model

For Fe I, we included the 2542 transitions with transition rates in the ASD, involving a total of 434 levels. Though more than 50% of the transitions are outside our spectral window, they may affect the level populations and were included. Our flux atlas was sufficient for producing absorption and stimulated emission rates for all but four M1 transitions between levels of the configuration  $3d^64s^2$ , which were approximated with a blackbody.

Figure 1 (bottom panel) shows a synthetic Fe I fluorescence spectrum at the observing conditions of comet Hyakutake (Meier et al. 1998). The strongest lines are predicted in the UV between ~340 and 390 nm. For the Fe I Monte Carlo iterations, the error bars of most lines (>99%) converge within 10<sup>4</sup> iterations. In Figure 3 (bottom), we show a comparison of our Monte Carlo uncertainty calculation versus the NIST accuracy ratings of the transition rates for 425 selected lines following the procedure derived for Ni I. Compared to Ni I, most of the strongest lines of Fe I exhibit a Monte Carlo uncertainty less than the ASD accuracy rating. For weak lines, the Monte Carlo uncertainty is generally comparable to or larger than the ASD uncertainty rating.

# 3.5. Total Model Uncertainties

For the archived data of C/1996 B2 (Hyakutake), the heliocentric velocity  $(-36.7\,\mathrm{km\,s^{-1}})$  leads to favorable fluorescence efficiencies. We calculated the fluorescence efficiencies of Ni I and Fe I across a grid of heliocentric velocities spanning  $v_h \pm 1\,\mathrm{km\,s^{-1}}$ . We consider the range of  $\pm 1\,\mathrm{km\,s^{-1}}$  an upper bound, as this covers a range of typical outflow velocities in comae and is larger than the thermal speed of Ni and Fe atoms at 270 K (0.2 km s<sup>-1</sup>). Within this range the average change in fluorescence efficiencies for all lines was 0.9% for Ni I and 1.5% for Fe I. Our total model uncertainties were thus obtained by adding in quadrature the uncertainty of the converged Monte Carlo iterations and the above heliocentric velocity sensitivity.

### 3.6. Benchmarking against Sungrazer Ikeya-Seki

As an additional check on the accuracy of the fluorescence model, we applied our model to two spectra of Fe I and Ni I collected during the perihelion passage of comet C/1965 S1 (Ikeya-Seki) in 1965. Two line lists are available from

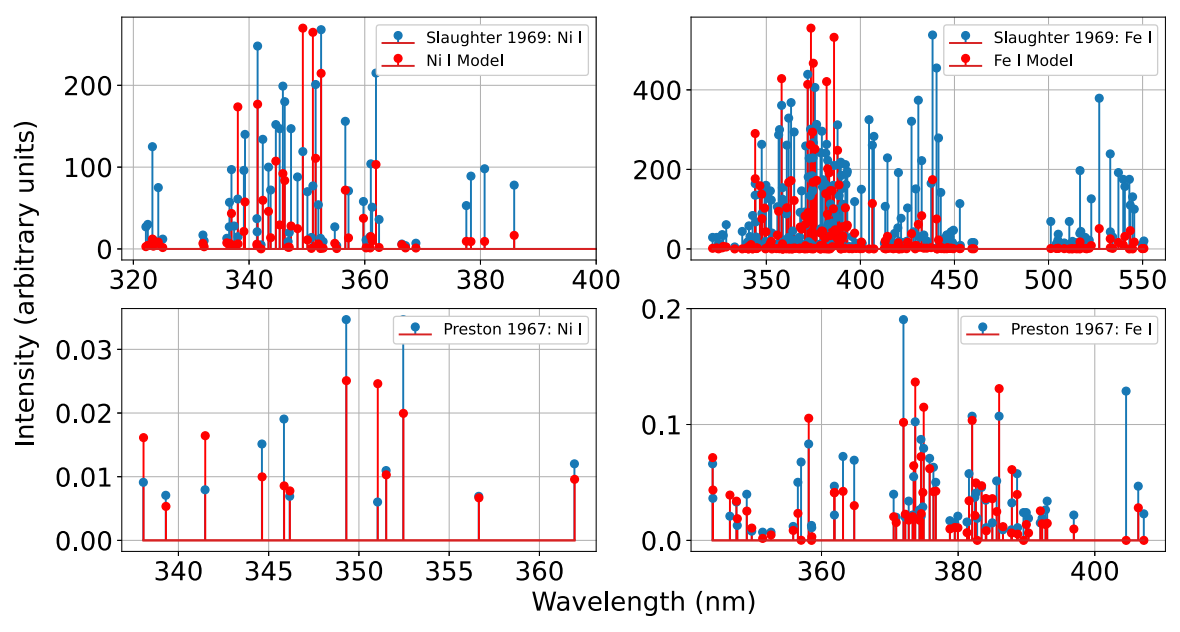


**Figure 4.** Comparison of Ni I (left) and Fe I (right) line intensities of our fluorescence model to the observed intensities of comet C/1965 S1 (Ikeya-Seki) as reported in Slaughter (1969) (top) and Preston (1967) (bottom). The model spectra are scaled via a linear fit of all present lines. Doppler line profiles were assumed for equilibrium temperatures derived from the heliocentric distances: 1067 (Slaughter 1969) and 818 K (Preston 1967).

Slaughter (1969) at  $30 R_{\odot}$  ( $v_h \sim 154 \,\mathrm{km \, s^{-1}}$ ) and Preston (1967) at  $\sim 13 R_{\odot}$  ( $v_h \sim 116 \,\mathrm{km \, s^{-1}}$ ).

Figure 4 shows the comparison of our model spectra and intensities of Fe I and Ni I lines reported by Slaughter (1969) and Preston (1967). The modeled spectra were scaled by a linear fit of modeled versus observed line intensity for all metal lines. The Ikeya-Seki spectra were recorded on photographic plates, and thus a direct comparison between the model versus observed intensities is difficult. Slaughter (1969) notes that agreement between expected and observed line intensities of a thorium-argon lamp agreed within a factor of 2. Preston (1967) reported intensities in terms of the local sky continuum, and thus we expect that their intensity scale may differ as a function of wavelength. We assume a similar factor of 2 scatter due to intensity calibration.

The best agreement between our model and the reported lines in the spectra of Ikeva-Seki is found for the spectrum collected at  $13 R_{\odot}$  by Preston (1967). The agreement with all observations, particularly the spectrum at  $30 R_{\odot}$  (Slaughter 1969), is improved significantly if a linear offset is included in the fit (assumed to account for reflected solar continuum). The large thermal temperature (T > 4000 K) in Ikeya-Seki may have introduced additional excitation mechanisms, but this effect would be more pronounced for the spectra of Preston (1967). The source of the disagreement between our model and the line list of Slaughter (1969) is not known, but it is likely that the strongest lines saturated the photographic plates, leading to a relative suppression of the weaker features in the scaling of our model to the observed line intensities. However, lines that were strong in the Ikeya-Seki spectra have appreciable g-factors in our models, and we thus consider this agreement as sufficient validation of our model.

# 3.7. Molecular Contamination

Near-UV and optical cometary spectra consist of reflected sunlight superimposed on many emission features of radicals.

To determine the reliability of our line identifications, we used the Planetary Spectrum Generator (PSG) to generate synthetic fluorescence spectra of the diatomic molecules OH, CN, C<sub>2</sub>, NH, and CH (Villanueva et al. 2018). The emission of metals, cations, and triatomics (e.g., C<sub>3</sub>), or prompt emission of OH, is currently unavailable in the PSG. Spectra were generated for production rates set to unity, which were then rescaled with respect to OH by the production rates measured by Meier et al. (1998) and Schleicher & Osip (2002). The combined molecular spectra were then manually rescaled by a single parameter to match our comet spectra. This procedure is not intended to accurately replicate the exact features in our comet spectra, but to elucidate sources of contamination in identified metallic lines. The molecular features are well spread across the orders of the echelle and make apparent the uncertainty of the wavelength calibration around some of the metallic features.

To aid future spectroscopy efforts, we have defined the following confidence scale for our line identifications. "A" ratings are stated for isolated lines with no strong nearby features and whose line profile is well fit. "B" ratings are listed for lines with one or more flaws, including possible molecular contamination or blends in the lab spectra. Lastly, "C" ratings are listed for lines with serious molecular contamination, poor fit, or low signal-to-noise ratio. For each letter grade, additional flags are shown in parentheses indicating the source of the molecular contamination, e.g., (CN).

# 4. Results

# 4.1. Detections of Ni I and Fe I Lines

The metal lines from atomic iron and nickel we identified in the spectrum of C/1996 B2 (Hyakutake) are listed in Table 2. Where possible, we have indicated if a line has previously been observed by Manfroid et al. (2021), by Guzik & Drahus (2021), or in the spectra of Ikeya-Seki (Slaughter 1969; Preston 1967). Ritz, comet, and lab wavelengths, observed and modeled intensities, upper/lower configuration information, and confidence ratings are also provided.

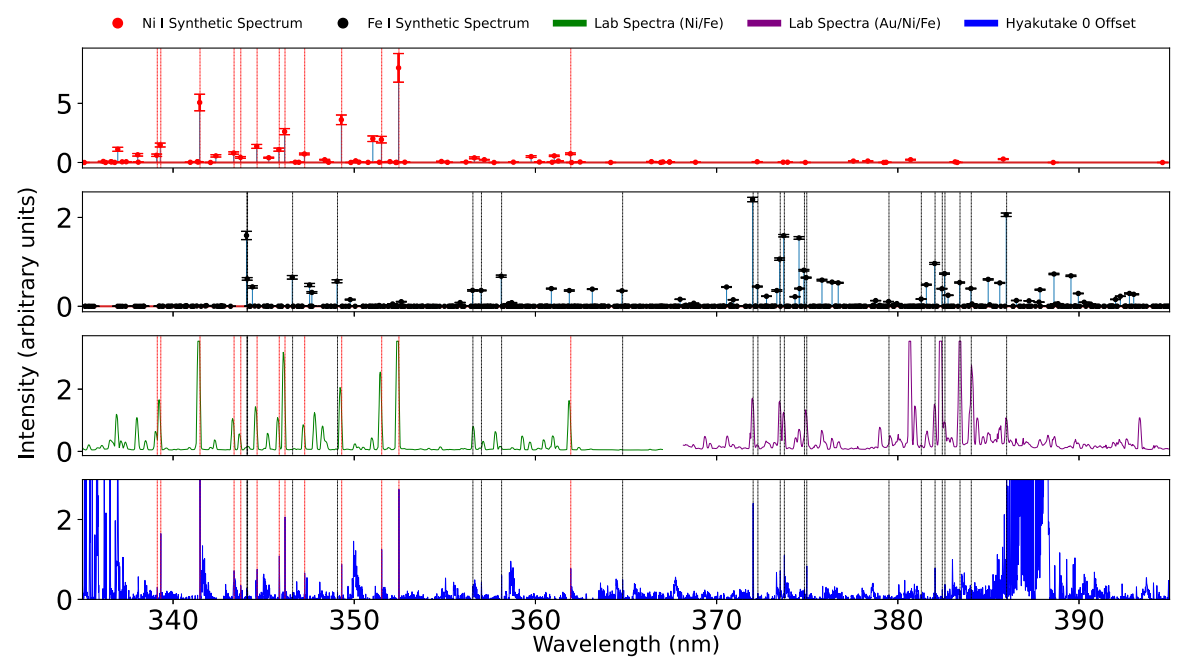
https://ssd.jpl.nasa.gov/horizons.cgi

Table 2 List of Observed Ni I and Fe I Lines

Species	$^{ m a}\lambda_{ m Ritz}$	$\lambda_{ m comet}$	$\lambda_{ m lab}$	$^{\mathrm{b}}I_{\mathrm{comet}}$	$g_{ m model}$	A Value	Lower Level	Upper Level	Confidence	SS	BOR	IS
Fe I	344.06	344.07	344.15	$38.6 \pm 15.44$	$0.89 \pm 0.05$	1.7 + 07	$3d^64s^2 \ a^5D_4$	$3d^6(^5D)4s4p(^3P) w ^5P_3$	A (Bl. Lab)	✓		<u>√</u>
Fe I	344.1	344.11	344.15	$18.5\pm7.4$	$0.35\pm0.02$	1.2 + 07	$3d^64s^2 \ a^5D_3$	$3d^6(^5D)4s4p(^3P) w ^5P_2$	A (Bl. Lab)	✓		✓
Fe I	346.59	346.6	346.6	$24.3 \pm 9.72$	$0.37\pm0.02$	1.2 + 07	$3d^64s^2 \ a^{5}D_1$	$3d^6(^5D)4s4p(^3P) z ^5P_1$	B (OH; Bl. Lab)	✓		✓
Fe I	349.06	349.07		$24.6 \pm 9.84$	$0.32\pm0.02$	6.1 + 06	$3d^64s^2 \ a^5D_3$	$3d^6(^5D)4s4p(^3P) z ^5P_3$	Α	✓		✓
Fe I	356.54	356.55	356.51	$47.6 \pm 19.04$	$0.2 \pm 0.01$	4.3 + 07	$3d^{7}(^{4}F)4s \ a^{5}F_{3}$	$3d^{7}(^{4}F)4p z^{3}G_{4}$	C	✓		✓
Fe I	357.01	357.02		$53.6 \pm 21.44$	$0.2 \pm 0.01$	6.8 + 07	$3d^{7}(^{4}F)4s \ a^{5}F_{4}$	$3d^{7}(^{4}F)4p \ w^{3}G_{5}$	A	✓		✓
Fe I	358.12	358.13		$84.7 \pm 33.88$	$0.38 \pm 0.01$	1.0 + 08	$3d^{7}(^{4}F)4s \ a^{5}F_{5}$	$3d^{7}(^{4}F)4p \ w \ ^{5}G_{6}$	B (CN)	✓		✓
Fe I	364.78	364.81		$69.6 \pm 27.84$	$0.2 \pm 0.01$	2.9 + 07	$3d^{7}(^{4}F)4s \ a^{5}F_{4}$	$3d^{7}(^{4}F)4p z^{5}G_{5}$	C (CH)	✓		✓
Fe I	371.99	372.01	372.0	$407.0 \pm 162.8$	$1.34 \pm 0.03$	1.6 + 07	$3d^64s^2 \ a^5D_4$	$3d^6(^5D)4s4p(^3P) w^5F_5$	B (NH)	✓		✓
Fe I	372.26	372.28		$22.0 \pm 8.8$	$0.25 \pm 0.01$	5.0 + 06	$3d^64s^2 \ a^5D_2$	$3d^6(^5D)4s4p(^3P) z ^5F_2$	C	✓		✓
Fe I	373.49	373.51	373.49	$101.0 \pm 40.4$	$0.59 \pm 0.01$	9.0 + 07	$3d^{7}(^{4}F)4s \ a^{5}F_{5}$	$3d^{7}(^{4}F)4p \ y^{5}F_{5}$	B (NH)	✓		✓
Fe I	373.71	373.74	373.7	$155.0 \pm 62.0$	$0.89 \pm 0.02$	1.4 + 07	$3d^64s^2 \ a^5D_3$	$3d^6(^5D)4s4p(^3P) w ^5F_4$	A	✓		✓
Fe I	374.83	374.85		$44.8\pm17.92$	$0.46\pm0.01$	9.2 + 06	$3d^64s^2 \ a^5D_1$	$3d^6(^5D)4s4p(^3P) w ^5F_2$	C (NH)	✓		✓
Fe I	374.95	374.98	374.95	$141.0 \pm 56.4$	$0.36 \pm 0.01$	7.6 + 07	$3d^{7}(^{4}F)4s \ a^{5}F_{4}$	$3d^{7}(^{4}F)4p \ y^{5}F_{4}$	B (NH)	✓		✓
Fe I	379.5	379.51		$16.0\pm6.4$	$0.06 \pm 0.0$	1.2 + 07	$3d^{7}(^{4}F)4s \ a^{5}F_{2}$	$3d^{7}(^{4}F)4p \ y^{5}F_{3}$	C	✓		✓
Fe I	381.3	381.3	381.27	$14.3\pm5.72$	$0.09 \pm 0.0$	7.9 + 06	$3d^{7}(^{4}F)4s \ a^{5}F_{3}$	$3d^6(^5D)4s4p(^3P) z ^3P_2$	C (Weak in Lab)			✓
Fe I	382.04	382.06	382.05	$111.0 \pm 44.4$	$0.54 \pm 0.01$	6.8 + 07	$3d^{7}(^{4}F)4s \ a^{5}F_{5}$	$3d^{7}(^{4}F)4p \ y^{5}D_{4}$	A	✓		✓
Fe I	382.44	382.45		$34.5\pm13.8$	$0.22\pm0.01$	2.8 + 06	$3d^64s^2 \ a^5D_4$	$3d^6(^5D)4s4p(^3P) z ^5D_3$	A	✓		✓
Fe I	382.59	382.6	382.58	$63.3 \pm 25.32$	$0.41\pm0.01$	6.0 + 07	$3d^{7}(^{4}F)4s \ a^{5}F_{4}$	$3d^{7}(^{4}F)4p \ y^{5}D_{3}$	A	✓		✓
Fe I	383.42	383.43	383.42	$37.0\pm14.8$	$0.3 \pm 0.01$	4.5 + 07	$3d^{7}(^{4}F)4s \ a^{5}F_{3}$	$3d^{7}(^{4}F)4p \ y \ ^{5}D_{2}$	A	✓		✓
Fe I	384.04	384.06	384.08	$41.4 \pm 16.56$	$0.22\pm0.01$	4.7 + 07	$3d^{7}(^{4}F)4s \ a^{5}F_{2}$	$3d^{7}(^{4}F)4p \ y \ ^{5}D_{1}$	A	✓		✓
Fe I	385.99	386.0	385.99	$502.0 \pm 200.8$	$1.15\pm0.02$	9.7 + 06	$3d^64s^2 \ a^5D_4$	$3d^6(^5D)4s4p(^3P) z ^5D_4$	C (CN)	✓		✓
Ni I	323.29	323.31	323.35	$153.0 \pm 61.2$	$0.58 \pm 0.08$	7.3 + 06	$3d^8(^3F)4s^2(^3F_4)$	$3d^8(^3F)4s4p(^3P)(^3G_5)$	Α	✓		✓
Ni I	339.1	339.13	339.09	$34.6 \pm 13.84$	$0.45\pm0.07$	6.6 + 06	$3d^8(^3F)4s^2(^3F_4)$	$3d^9(^2D)4p^3F_4$	B (NH)	✓		✓
Ni I	339.3	339.32	339.27	$232.0 \pm 92.8$	$1.08 \pm 0.12$	2.4 + 07	$3d^9(^2D)4s(^3D_3)$	$3d^9(^2D)4p(?)_3$	B (NH)	✓	✓	✓
Ni I	341.48	341.49	341.46	$494.0 \pm 197.6$	$3.69 \pm 0.51$	5.5 + 07	$3d^9(^2D)4s(^3D_3)$	$3d^9(^2D)4p(^3F_4)$	A	✓	✓	✓
Ni I	343.36	343.37	343.33	$101.0 \pm 40.4$	$0.59 \pm 0.07$	1.7 + 07	$3d^9(^2D)4s(^3D_3)$	$3d^9(^2D)4p(^3F_3)$	A	✓		✓
Ni I	343.73	343.74	343.71	$49.2 \pm 19.68$	$0.31 \pm 0.05$	4.4 + 06	$3d^8(^3F)4s^2(^3F_4)$	$3d^8(^3F)4s4p(^3P)(^5F_4)$	C	✓		✓
Ni I	344.63	344.64	344.61	$106.0 \pm 42.4$	$1.0\pm0.12$	4.4 + 07	$3d^9(^2D)4s(^3D_2)$	$3d^9(^2D)4p(^3D_2)$	A	✓	✓	✓
Ni I	345.85	345.86	345.82	$153.0 \pm 61.2$	$0.8 \pm 0.1$	6.1 + 07	$3d^9(^2D)4s(^3D_1)$	$3d^9(^2D)4p(^3F_2)$	A	✓	✓	✓
Ni I	346.17	346.18	346.14	$291.0 \pm 116.4$	$1.9 \pm 0.19$	2.7 + 07	$3d^9(^2D)4s(^3D_3)$	$3d^{8}(^{3}F)4s4p(^{3}P)(^{5}F_{4})$	A	✓	✓	✓
Ni I	347.25	347.27	347.23	$93.5 \pm 37.4$	$0.53 \pm 0.05$	1.2 + 07	$3d^9(^2D)4s(^3D_2)$	$3d^9(^2D)4p(?)_3$	A	✓		✓
Ni I	349.3	349.31		$125.0 \pm 50.0$	$2.64 \pm 0.3$	9.8 + 07	$3d^9(^2D)4s(^3D_2)$	$3d^9(^2D)4p(^3P_1)$	С	✓	✓	✓
Ni I	351.51	351.52	351.48	$176.0 \pm 70.4$	$1.41 \pm 0.2$	4.2 + 07	$3d^9(^2D)4s(^3D_2)$	$3d^9(^2D)4p(^3F_3)$	A	✓	✓	✓
Ni I	352.45	352.47	352.43	$388.0 \pm 155.2$	$5.83 \pm 0.89$	1.0 + 08	$3d^9(^2D)4s(^3D_3)$	$3d^9(^2D)4p(^3P_2)$	A	✓	✓	✓
Ni I	361.94	361.95	361.9	$109.0 \pm 43.6$	$0.54 \pm 0.05$	6.6 + 07	$3d^9(^2D)4s(^1D_2)$	$3d^9(^2D)4p(^1F_3)$	A	✓	✓	✓

Notes. All wavelengths are reported as nm in standard air. Einstein A-values are written as  $m + n \equiv m \times 10^n$ . Lines previously observed in solar system comets (SS; Manfroid et al. 2021), 2I/Borisov (BOR; Guzik & Drahus 2021), or Ikeya-Seki (IS; Preston 1967; Slaughter 1969) are shown by a "\sqrt{"}" symbol. Unknown LS term identifications for a given J-level are indicated by a ? symbol.

a  $\lambda_{\text{Ritz}}$  are calculated (in vacuum) from level energies and converted to air wavelengths using the formulae in Morton (2000).
b  $I_{\text{comet}}$  reported in units of  $10^{-24} \, \text{J s}^{-1} \, \text{cm}^{-2}$  after integration over a Gaussian profile fit to each line.
c The *g*-factors are reported in units of  $10^{-21} \, \text{J s}^{-1} \, \text{particle}^{-1}$ ; uncertainties are taken as the quadrature sum of heliocentric velocity sensitivity (see Section 3.5) and standard deviation of  $10^6 \, \text{Monte}$  Carlo iterations (see Section 3.2).



**Figure 5.** From top to bottom: (1) Ni I synthetic spectrum (red) at the orbital conditions of Hyakutake, (2) Fe I synthetic spectrum (black) at the orbital conditions of Hyakutake, (3) laboratory spectrum of an Ni/Fe probe at 3 cm depth in the CTH plasma apparatus (shot 18,112,918, frame 88, green) and laboratory spectrum of an Au/Ni/Fe probe at 6 cm depth in the CTH plasma apparatus (shot 18113013, frame 81, purple), (4) observation spectrum of Hyakutake (blue). Ni I (red) and Fe I (black) lines identified in the comet spectrum are indicated by vertical dashed lines in the lab and comet spectra.

We identified 14 Ni I emission lines by comparison with the fluorescence model and lab measurements. Within these 14 lines, 13 were found in both the lab and comet spectra, with the remaining line identified by comparison with our model exclusively. In some cases, deviations between the known air wavelengths of the observed lines and their wavelength in the comet spectrum are ~0.02 nm. These wavelength differences were noted by A'Hearn et al. (2015a) as resulting from calibration of the numerous orders of the echelle spectrograph. However, the direction and scale of the wavelength shift(s) are obvious when comparing heights and positions of several nearby metal and/or molecular features.

Figure 5 shows a comparison of our modeled nickel and iron g-factors, laboratory spectra, and comet spectrum. Ni I (red) and Fe I (black) spectra are shown as stick plots, with error bars reported from the Monte Carlo procedure described previously. Lines confirmed in the comet spectrum are indicated by dashed red (Ni I) or black (Fe I) vertical lines. For the laboratory spectra, two data sets are shown: spectra from erosion of an Ni/ Fe probe (green) and that of an Au/Ni/Fe probe (purple). Spectra of the Au/Ni/Fe probe show enhanced Fe emission compared to the pure Ni/Fe plasma, due to rapid erosion of the gold/nickel layers to expose the underlying stainless steel. As the poor broadband wavelength calibration in the spectral range of the Ni/Fe spectrum (green) led to a systematic shift of approximately -0.06 nm blueward for most lines, all  $\lambda_{lab}$ values for Table 2 were extracted from the Au/Ni/Fe spectra where available.

A total of 28 Ni I lines were reported by Manfroid et al. (2021), 14 of which were observed in the centered Hyakutake spectrum. The nine lines of Ni I observed in 2I/Borisov by Guzik & Drahus (2021) were all present in the spectrum of Hyakutake. We identified 22 Fe I lines in the spectrum of Hyakutake, 21 of which were also in the line list of Manfroid et al. (2021). The additional line was also found in Ikeya-Seki and is among the weakest iron features in the Hyakutake

spectrum. The nondetection of this line in the sample of Manfroid et al. (2021) is not surprising given Hyakutake's proximity to Earth ( $\Delta=0.11$  au), large activity ( $Q_{\rm H_2O}>10^{29}$  mol s<sup>-1</sup>; Meier et al. 1998), and favorable heliocentric velocity. We note that every metal line detected in Hyakutake was also observed in Ikeya-Seki by Preston (1967) and/or Slaughter (1969).

Sixteen (73%) of the comet's Fe I lines were also identified in the lab spectra, though many more Fe I and Fe II features were apparent between 200 and 300 nm in the lab spectra. The electron temperature  $T_{\rm e} > 20~{\rm eV}$  led to a significant population of Fe II arising from ionization and excitation of iron eroded from the stainless steel probe underneath the gold and nickel coatings. In the comet spectrum, Fe I lines are generally weaker than those of Ni I, and we find no evidence of Fe II (see Section 4.2).

The observed metal emission lines are dipole-allowed transitions from the excited odd configurations of the form  $3d^{x}(x-1)4p$  and  $3d^{x}(x-1)4s4p$  to the ground and metastable configurations  $3d^x4s$  and  $3d^x4s^2$ . In Figure 6 we show Grotrian diagrams of Ni I and Fe I, where observed transitions are indicated by diagonal red lines. From our fluorescence models, we find no significant population of highly excited even-parity states that would indicate that any observed emission lines from highly excited even-parity configurations would be produced by nonfluorescence mechanisms. Similarly, we found no transitions in the comet spectrum that cannot be explained by absorption from the ground or metastable levels; the spectrum is fully consistent with fluorescence of atomic Ni and Fe. The average agreement between our modeled fluorescence efficiencies and the observed strengths of the cometary metal features is within a factor of  $\sim 2$ .

As electron impact can populate higher excited states compared to fluorescence, the lab spectra exhibit many transitions, e.g.,  $3d^84s4d \rightarrow 3d^84s4p$  transitions in Ni I, that are inaccessible via absorption alone. Transitions common to

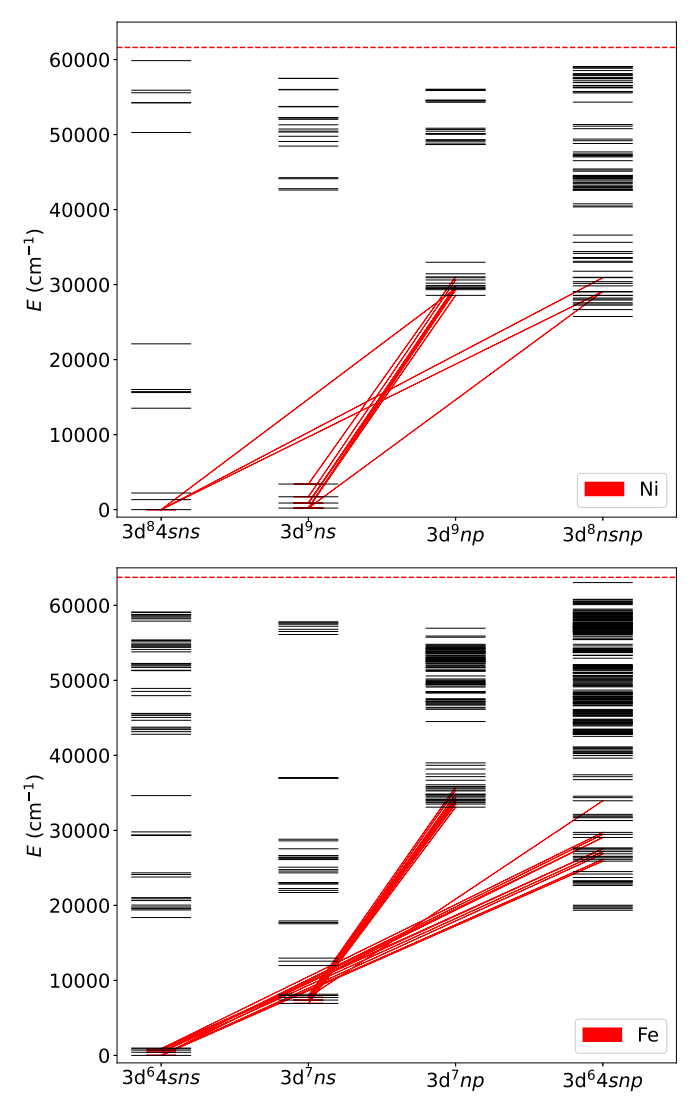


**Figure 6.** Grotrian diagrams of Ni I (top) and Fe I (bottom) showing the observed emission lines of each element as diagonal red lines. Ionization limits are shown as horizontal dashed lines. Many lines are known for each element (522 for Ni, 2539 for Fe), but only the observed lines are shown for clarity.

both the lab and comet spectra are typically the strongest transitions in the lab spectra, including the  $\lambda = 341.48$  nm and  $\lambda = 352.45$  nm lines of the form  $3d^{9}4p \rightarrow 3d^{9}4s$ . The upper levels of these transitions are accessible by both photon- and electron-impact excitation of the ground configuration.

According to the fluorescence model, the first six levels of Ni I above ground have populations comparable to the ground state. For Fe I, the metastable levels also have sizable populations, but neither Ni I nor Fe I is predicted to have observable emission in the infrared regime.

### 4.2. Searches for Other Metal Emission

We searched Hyakutake's spectrum for the emission of Fe II and Ni II; no matches in both wavelength and model intensity were found. We also searched for lines belonging to neutral and singly ionized metals present in Ikeya-Seki and dust grains: Al, Ca, Co, Cr, Cu, Mg, Mn, Na, Zn, and V.

Searches for Na I emission were hopeful considering the substantial g-factors for the 589 nm doublet on the order of 5–10 photons s<sup>-1</sup> particle<sup>-1</sup> (Cremonese et al. 1997) and its

detection in the tail of Hyakutake by Wyckoff et al. (1999). In comparison, the strongest line of Ni I in the present spectrum at 341.48 nm has a fluorescence efficiency  $g = 3.7 \times 10^{-21}$  J s<sup>-1</sup> particle<sup>-1</sup> =  $6 \times 10^{-3}$  photons s<sup>-1</sup> particle<sup>-1</sup>.

Other possible Na I lines in the present wavelength region are driven by emission from autoionizing levels that are unlikely to be populated by absorption alone. Models with numerous subsets of levels were computed, and g-factors for lines around  $\sim\!390$  nm are several to many orders of magnitude weaker than the doublet at 589 nm. Thus, we expect no sodium emission within the 300–400 nm window. For each element/ion above we computed g-factors considering only levels beneath the first ionization potential, as higher-lying levels are likely to be autoionizing. No matches for wavelength and relative intensity were found.

We draw attention to a particularly strong and sharp line at 416.68 nm for which no emission lines produced by our models were an appropriate match. Comparisons to data in the ASD suggest V I or Cu II, but these two transitions lack A-values, and both are transitions between two excited states, i.e., they are likely weak at 1 au. A possible (prompt) molecular origin is NH, though the transition rate for this particular transition is weak (Fernando et al. 2018).

#### 4.3. Production Rates and Abundances

Spectra were taken at various spatial offsets in the Hyakutake observations of Meier et al. (1998), but there is great uncertainty in photocenter location with respect to the nucleus for each offset observation. We focused our analysis on the centered observation and derived column densities (averaged over the slit) using the relation

$$n_{\rm col.} = \frac{F_{ij}}{g_{ii}} \frac{4\pi\Delta^2}{A_{\rm ap.}},\tag{10}$$

where  $F_i$  is the observed cometary flux from line  $\lambda_{ij}$ ,  $A_{\rm ap.}$  is the sky-projected slit size (68 × 580 km²),  $\Delta$  is the geocentric distance, and  $g_{ij}$  is the calculated fluorescence efficiency (Equation (7)). Column densities,  $n_{\rm col.}$ , were calculated from Equation (10) as the geometric mean of the column densities derived from all observed metal features. From our mean observed/model line ratios (Figure 7) and the uncertainties of our calculated g-factors we find  $n_{\rm Ni} = 1.17^{+0.17}_{-0.14} \times 10^{10}$  cm $^{-2}$  and  $n_{\rm Fe} = (1.66 \pm 0.06) \times 10^{10}$  cm $^{-2}$ .

Assuming a gas expansion velocity of  $v = 0.85 R_h^{-1/2}$  km s<sup>-1</sup> (Cochran & Schleicher 1993), we calculate the production rate of these metal atoms using Haser models (see the recent translation in Haser et al. 2020) implemented in the Small Body Python (*sbpy*) code (Mommert et al. 2019). The use of a Haser model to derive production rates in this context requires several assumptions. For species produced via dissociation or fragmentation (as expected for nickel and iron), each fragment receives a velocity kick (distribution), which may result in a higher outflow velocity than that derived from the assumed relation above. Currently, the production mechanisms and possible parent loss mechanisms are unknown, and application of a vectorial model (Festou 1981) would not improve the accuracy of our results.

We have attempted to minimize the inaccuracies of our Haser models by restricting our parameter space and deriving daughter scale lengths from known photoionization rates of nickel and iron. Following a similar procedure to Guzik & Drahus (2021),

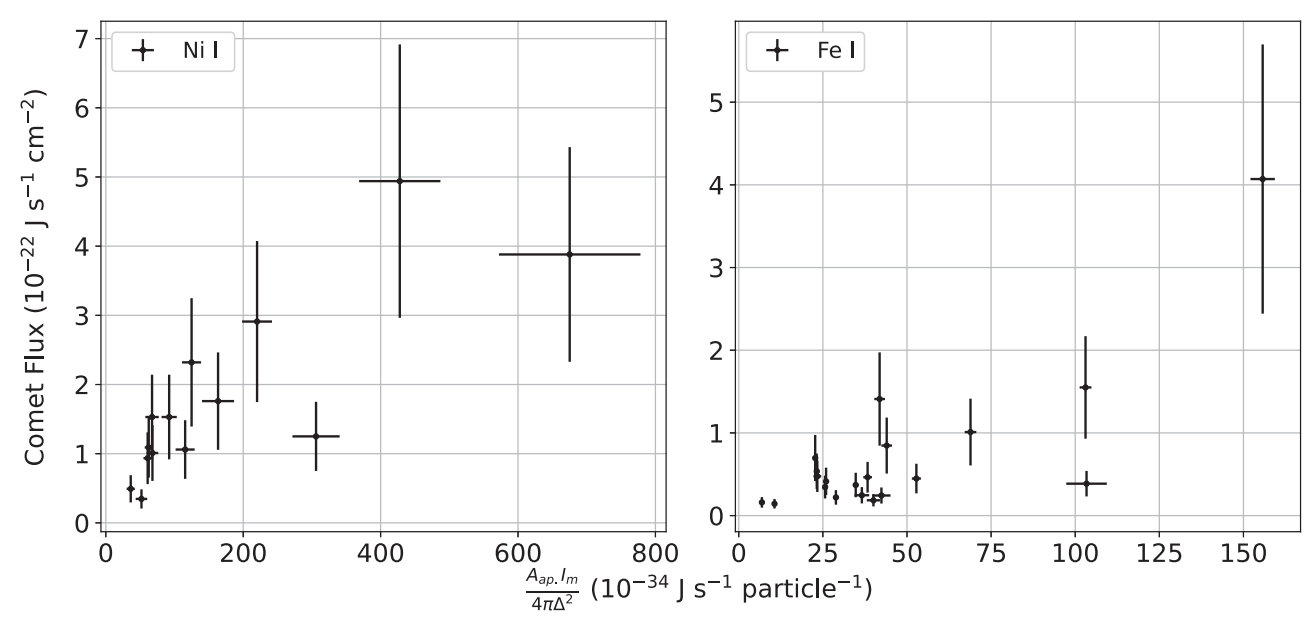


Figure 7. Comparison of modeled and observed line intensities of Ni I (left) and Fe I (right). Model error bars are taken as the quadrature sum of the Monte Carlo uncertainty and the sensitivity to heliocentric velocity (see text), and an absolute error for the observed intensities was assumed to be  $\pm 40\%$  (Meier et al. 1998).

we used the known lifetimes at 1 au during solar minimum (Huebner & Mukherjee 2015) for Ni I  $(1.06 \times 10^6 \, \text{s})$  and Fe I  $(5.94 \times 10^5 \, \text{s})$  to derive daughter scale lengths of  $8.92 \times 10^5$  km and  $5.01 \times 10^5$  km, respectively. For the unknown parent, we restricted the scale length to  $l_{\text{parent}} < 1000$  km, in line with the procedure reported by Guzik & Drahus (2021).

Without additional spatial information, we are limited to restricting the production rates to a range within the bounds calculated from the uncertainty of the observed total numbers of particles. We iterated the Haser models over a grid of parent scale length and production rate, after which the Haser column densities were integrated over the rectangular aperture. Using the observed total number of particles within our aperture ( $N = A_{\rm ap.} \times n_{\rm col.}$ ,  $N_{\rm Ni} = 4.6^{+0.7}_{-0.5} \times 10^{24}$ ,  $N_{\rm Fe} = 6.5^{+0.3}_{-0.2} \times 10^{24}$ ), we narrowed the range of production rates for nickel and iron to  $Q_{\rm Ni} = (2.6-4.1) \times 10^{22} \ {\rm s}^{-1}$  and  $Q_{\rm Fe} = (0.4-2.8) \times 10^{23} \ {\rm s}^{-1}$ .

#### 5. Discussion

# 5.1. Comparison of Hyakutake to the Broader Sample of Comets

Due to their large fluorescence efficiencies, neutral iron and nickel emission were observed for production rates as low as  $\sim\!\!8\times10^{21}\,\mathrm{s}^{-1}$  by Manfroid et al. (2021). Our production rates are comparable to those observed in other solar system comets on the order of  $\sim\!10^{22}\,\mathrm{s}^{-1}$ , with the large uncertainties stemming from the lack of spatial information and intensity calibration of the echelle spectra. Hyakutake was a particularly active comet with  $Q_{\rm H_2O}>2.2\times10^{29}$  mol.  $\rm s^{-1}$  (Meier et al. 1998), and our mean iron production rate of  $Q_{\rm Fe}=1.6\times10^{23}\,\mathrm{s}^{-1}$  is comparable to the most active comet observed by Manfroid et al. (2021), C/2016 R2 (Pan-STARRS). With a mean value of  $Q_{\rm Ni}=3.4\times10^{22}\,\mathrm{s}^{-1}$ , the nickel production rate in Hyakutake is in line with the majority of the already-observed solar system comets.

The Ni/Fe abundance ratios reported for solar system comets (in  $\log_{10}$ ) span the range -0.68 to +0.6. From our production rates, the Ni/Fe abundance observed in Hyakutake (in  $\log_{10}$ , hereafter denoted [Ni/Fe]) ranges from -0.98 to

-0.03. This range is dominated by additional uncertainties introduced via the lack of constraint on parent scale length in the present work. In this context, it is more appropriate to derive an [Ni/Fe] abundance from the column densities, which yields  $[Ni/Fe] = -0.15 \pm 0.07$ . This Ni/Fe abundance differs significantly from both solar (-1.25) and Ikeya-Seki (-1.1)ratios, where the fluorescing material is sourced from the bulk composition and from dust collected from 1P/Halley, where  $\log_{10}(\text{Ni/Fe}) = -1.1$  (Jessberger et al. 1988). Both 0" and 2" spectra from the archived observations of Hyakutake were analyzed independently by Hutsemékers et al. (2021),8 who found Ni/Fe between -0.07 and -0.14 (depending on the offset) using a fluorescence model with restrictions on the input atomic data. These values overlap with the present work within the uncertainties and suggest that the most important transitions were common to both sets of models.

Figure 8 shows a comparison of abundance ratios in Hyakutake (dashed red lines) to comets studied by Manfroid et al. (2021) and Guzik & Drahus (2021). Abundance ratios for Hyakutake were derived from the geometric mean of the production rate ranges reported previously and are shown as dashed vertical red lines. Abundance ratios for 2I/Borisov are shown as dashed black lines where applicable. Hyakutake appears relatively depleted in Ni with respect to both OH and CN. Using our mean Fe production rate  $(1.06 \times 10^{23} \text{ s}^{-1})$ , Hyakutake's Fe/OH and Fe/CN abundances are similar to the majority of solar system comets.

Nickel and iron have been observed in comets of all dynamical families at distances between 0.68 and 3.25 au. The [Ni/OH] abundance ratio of Hyakutake (-6.8) is most similar to the Jupiter-family comet 103P/Hartley 2 ([Ni/OH] = -6.72) and the dynamically new Oort cloud comet C/2003 K4 (LINEAR) with [Ni/OH] = -6.68. Similarly, the [Ni/CN] ratio (-3.99) is smaller than most of the comets studied by Manfroid et al. (2021) but is again comparable to 103P (-3.79) and C/2003 K4 (-3.96). The presence in 2I/Borisov implies a common organometallic chemistry during planet formation that may be largely

Published during the review process of the present work.

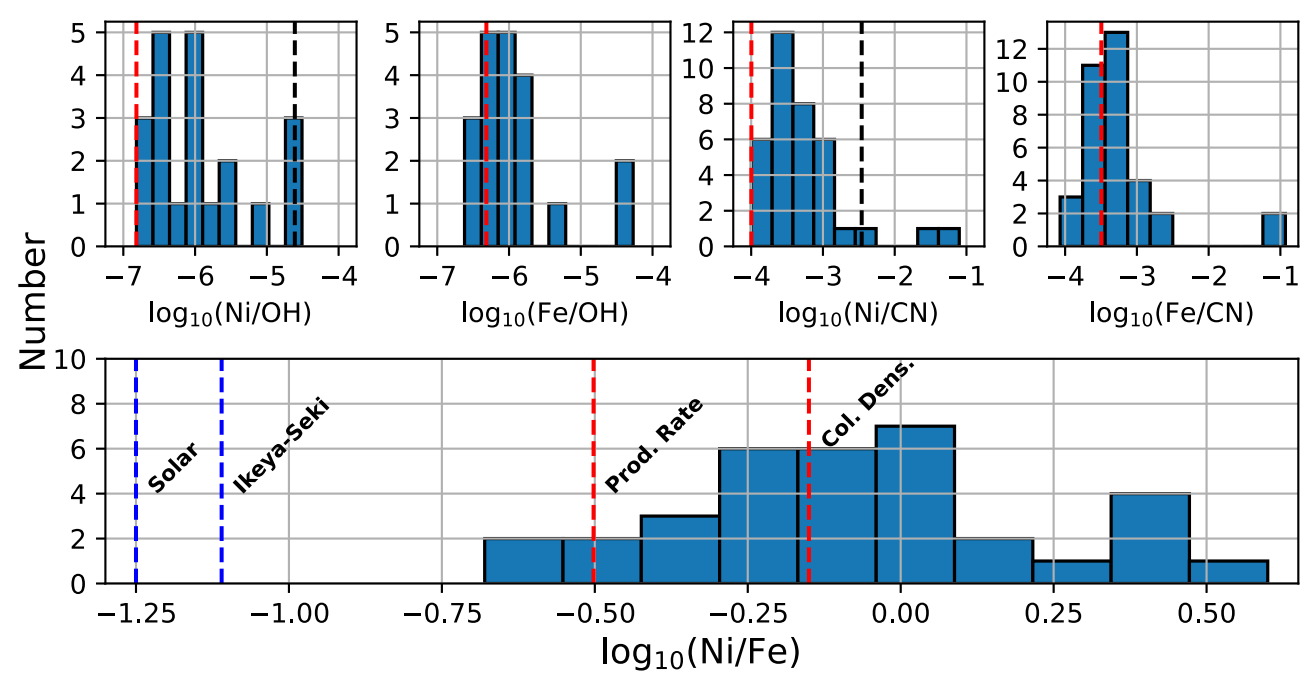


Figure 8. Histograms (# bins = 10) of [Ni/OH], [Fe/OH], [Ni/CN], [Fe/CN], and [Ni/Fe] in  $\log_{10}$  for all comets with measured nickel and iron production rates to date. Ni, Fe, OH, and CN production rates were taken from Manfroid et al. (2021), Meier et al. (1998), Schleicher & Osip (2002), and Guzik & Drahus (2021). Ratios for 2I/Borisov are indicated by dashed black vertical lines, and ratios for Hyakutake are indicated by red dashed lines. Metal/molecule abundance ratios for Hyakutake were derived from the geometric mean of the constrained range of production rate in Hyakutake; for Ni/Fe, ratios derived from the mean production rates and column densities are both shown.

independent of dust and volatile formation chemistry given the differences between most solar system comets and the Ni/OH and Ni/CN abundances of 2I/Borisov. The presence in the CO-rich comet C/2016 R2 (Pan-STARRS; McKay et al. 2019) is puzzling considering that the production rates of nickel and iron in C/2016 R2 are among the largest to date. The high metal production and low water production in C/2016 R2, in addition to some comets having enhanced water production from icy grain sublimation, suggest that Ni/OH or Ni/H<sub>2</sub>O abundance ratios present a poor categorization of the metallic inventory. It is clear that the magnitudes of nickel and iron production are correlated to overall gas and dust production (Manfroid et al. 2021), but the driving mechanism behind metal atom production in the coma has yet to be confirmed.

# 5.2. Chemical Origins and Physical Processes

Detection of gas-phase nickel and iron vapor around comets presents a new intersection of chemistry, planetary science, and atomic physics. It is well known that complex molecules form in planetary disks in the gas phase and on grain surfaces (Öberg et al. 2017), and there are indications that transition-metal chemistry is gaining interest (e.g., Kerkeni et al. 2019 and references therein). Both the parent molecule(s) and the excitation process of the atomic metals are currently unknown. However, it is possible to constrain likely parents and production mechanisms considering the totality of available laboratory studies.

First, we consider the spatial distribution of the nickel and iron emission. A'Hearn et al. (2015a) noted several complications in the exact positions of the pointings: the guiding for the Hyakutake spectra was carried out using visible wavelengths, and it is expected that spatial offsets in the UV are likely  $\sim\!100\,\mathrm{km}$  larger, with variations of order tens of kilometers within a given spectral range. While tracking the comet for the 7" offset observation, a fragment was visually identified and noted in the observing log.

We therefore expect emission from the 7" spectrum to be enhanced from the presence of a localized transient within the field of view (A'Hearn et al. 2015a). It is likely that the true spatial offset differs for each offset observation. Therefore, we use these offset spectra only to comment on a qualitative comparison of the spatial distributions.

Spectra of comet 103P/Hartley 2, collected at multiple orientations by Manfroid et al. (2021), indicate that the distribution of nickel and iron is isotropic, and the spatial distribution follows a 1/r profile indicating either direct sublimation from the nucleus or a short-lived parent. We investigated the presence of our Ni and Fe lines from the centered observation in the spectra collected at 2", 7", and 10". Figure 9 (top) shows the spatial distribution of Ni and Fe lines in the present work compared to OH and NH emission from Meier et al. (1998). For each species, we normalized the emission to 1 at I(r = 0), which is shown at the expected offset distance (70 km) in Meier et al. (1998). We see large differences between the spatial distributions of Ni and Fe lines compared to the molecular fluxes of OH and NH bands from Meier et al. (1998). Metal features appear comparatively more enhanced than the molecular features at 7" from the presence of the local transient.

Schleicher & Osip (2002) proposed that sublimation of small icy grains in the coma led to enhancement of the water production in Hyakutake, and the more recent study of Sunshine & Feaga (2021) elaborates on the contributions of icy grain sublimation to water vapor around 103P/Hartley 2, which shows an asymmetric H<sub>2</sub>O profile. The differences between water ice and water vapor spatial distributions are clearly distinguishable in imaging from A'Hearn et al. (2011) and Protopapa et al. (2014). However, the Fe I profile reported by Manfroid et al. (2021) for 103P was found to be isotropic. If icy grains in the coma contained the Ni and Fe parents, the

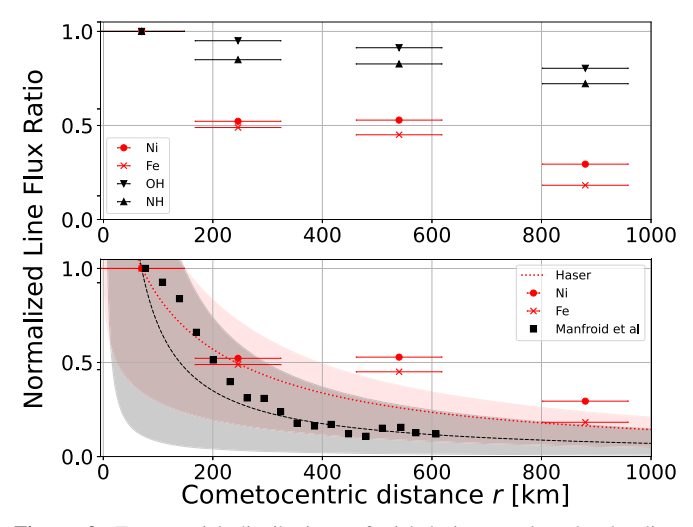


**Figure 9.** Top: spatial distributions of nickel, iron, and molecular lines normalized to 1 at photocenter (r = 70 km). Ni (circles) and Fe (crosses) flux ratios were taken as the mean of I(r)/I(r = 70) of the seven Ni and four Fe (7) lines present at all four distances. OH (downward-pointing triangles) and NH (upward-pointing triangles) fluxes and cometocentric distances were digitized from Meier et al. (1998). Bottom: comparison of present Ni and Fe lines (red circles and red crosses, respectively) to the Fe line profile of comet 103P/H Hartley 2 (squares, shifted +70 km) reported in Manfroid et al. (2021). A 1/r profile normalized to 1 at r = 70 km is shown in black, with gray contours indicating position uncertainty of the 0'' pointing of Hyakutake. A Haser model of atomic Ni is shown as a dotted red line, assuming daughter and parent scale lengths of  $8.9 \times 10^5 \text{ km}$  and 200 km, respectively, with red shaded contours showing the uncertainty of the Ni Haser spatial distribution assuming the uncertainty of the photocenter pointing at 0''.

profiles would be more similar to those observed for, e.g., OH and NH. The isotropy of the metal emission and the sharp profiles suggest that the parents of Ni and Fe are not related to icy grain sublimation in the coma.

Figure 9 (bottom) shows a comparison of the present Ni and Fe flux profiles in Hyakutake and an Fe profile from 103P/Hartley 2 digitized from Manfroid et al. (2021). A 1/r profile (black) and a Haser model (red) are both shown, with contours showing the effect of pointing uncertainty at 0''. Ignoring the enhanced fluxes at 7'' (540 km) due to the possible localized transient, we find reasonable agreement for a simple Haser model with a parent scale length of order hundreds of kilometers, consistent with the assertion of a short-lived parent or direct release from the nucleus. Without additional insights into the accuracies of the spatial offsets, a more refined analysis of the spatial distribution in Hyakutake is unreliable.

Two possible parents have been proposed thus far: metal carbonyls, and metal-bonded polycyclic aromatic hydrocarbons (hereafter MBPAHs). Iron and nickel carbonyls (Fe(CO)<sub>5</sub> and Ni(CO)<sub>4</sub>) have been suggested as possible parents by Manfroid et al. (2021), and their chemical model suggests sublimation temperatures in the range 74–108 K, comparable to CO (81 K), explaining the production of nickel and iron out to several au. Carbonyl photochemistry has attracted attention in the laboratory as a target for ultrafast photoionization studies; see, e.g., Distefano (1970), Leadbeater (1999), Fuss et al. (2001), and the most recent study of iron carbonyl by Cole-Filipiak et al. (2021). Kotzian et al. (1989) reported absorption cross sections for chromium, iron, and nickel carbonyls (anchored to absolute scale between 224 and 237 nm depending on species) and investigated the excited populations of removed CO groups.

Using the reported absorption cross sections of Kotzian et al. (1989) and assuming their absolute scaling applies across the full 200–350 nm range, we estimate the average number of dissociations per second experienced by a single carbonyl molecule in the presence of solar radiation (at 1 au). As a caveat, the UV absorption cross sections of the intermediate complexes are not known. We assume that said intermediates have the same UV absorption characteristics as the initial parent carbonyls and that each UV absorption removes only one CO group, though UV absorption can remove as many as three or four CO groups at once (Leadbeater 1999).

Convolution with our solar spectrum and integration over the 200–350 nm data from Kotzian et al. (1989) yield 0.03 dissociations per second ( $\sim 30~s$ /ionization) for both nickel and iron carbonyls. Assuming a constant velocity of 1 km s<sup>-1</sup>, the initial carbonyl molecules would be fully stripped to bare Ni/Fe within 120–150 km, a distance consistent with the spatial distributions observed thus far. Assuming that iron/nickel carbonyls are the precursors to atomic iron/nickel in the coma, successive absorption of UV photons is thus a plausible production mechanism. The similarity in dissociations per second for both metal carbonyls implies that differences in UV absorption characteristics are not the source of the deviation from solar Ni/Fe abundance. Future studies on the intermediate complexes such as Fe(CO)<sub>4</sub> would be required to validate the assumptions in the above estimation.

We searched for laboratory experiments that would support the possibility of dissociative processes that would result in the direct production of Ni or Fe in excited states, such as electron-impact dissociation or photodissociative excitation. Fe I emission was identified from electron-impact dissociative emission of iron carbonyl at 50 eV (Ribar et al. 2015). Their apparatus operates in the single collision regime, where only emission from the immediate dissociation and not electron-impact excitation of the fragments is observed before the fragments exit the field of view. Ribar et al. (2015) reported emission lines of Fe I from emissive dissociation of iron carbonyl, including the strongest Fe I emission in the spectrum of Hyakutake at  $\sim$ 372 nm. However, other strong transitions are notably absent. The preponderance and variety of Fe I lines identified to date in comet spectra, the sensitivity to heliocentric velocity (to be discussed in Section 5.3), and the good agreement with fluorescence models suggest that prompt emission is a small or nonexistent contribution to the observed metal emission features.

MBPAHs have been proposed to exist in the interstellar medium (ISM; see, e.g., Klotz et al. 1996) and are an alternative proposed precursor to atomic nickel/iron. Transition-metal astrochemistry is an active area of research, and there are indications that metals may play an important role in synthesizing known organic compounds (Fioroni 2014) and depleting metal abundances (in particular, Ni<sup>+</sup>) in the ISM (Kerkeni et al. 2019). At present, no possible Ni- or Fe-bearing PAH precursor molecules have been identified, though the abundance of Ni with respect to water is comparable to the abundance of PAHs with respect to water,  $log_{10}[PAH/H_2O] \approx -6$  (Klotz et al. 1996). One can expect that an MBPAH parent, if truly the precursor of gasphase metals in comae, would most likely be verified by a (cryogenic) sample return mission, or infrared spectroscopy of the parent informed by quantum chemical structure calculations. Embedded ions have been observed to induce frequency shifts in PAH molecules (see, e.g., experiments on Cu<sup>+</sup> in quinoline

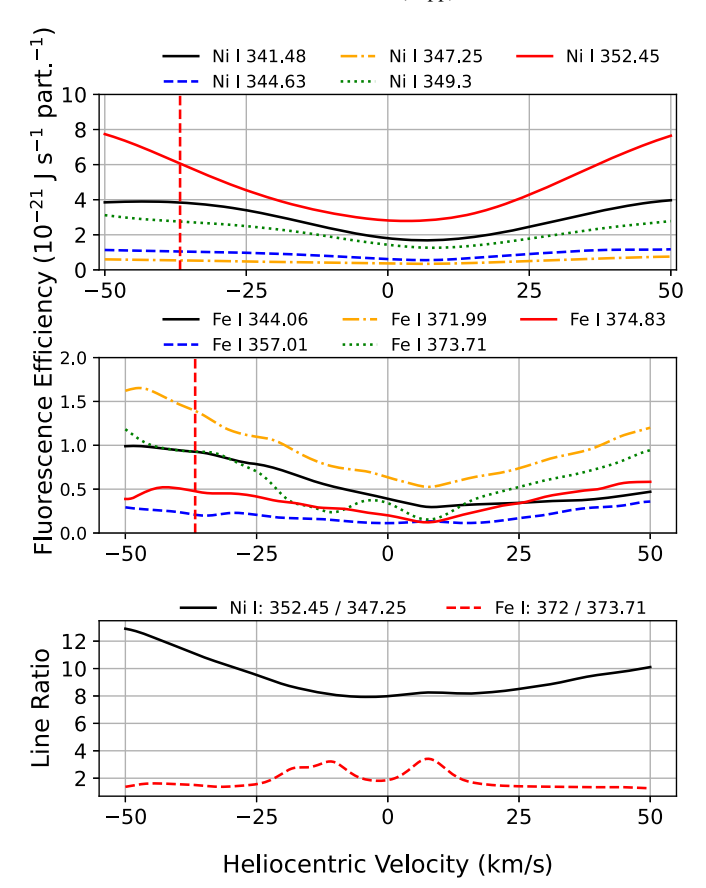


**Figure 10.** Sensitivity of our modeled fluorescence efficiencies for some representative Ni I lines (top) and Fe I lines (middle) to heliocentric velocity, and (bottom) example velocity-sensitive line ratios for Ni I (black) and Fe I (red). Efficiencies were calculated for a heliocentric distance of 1 au. The heliocentric velocity of Hyakutake (-36.7 km s<sup>-1</sup>) is shown as a vertical dashed line.

complexes; Gao et al. 2016), but it is unknown whether similar differences are observed in nickel/iron-bearing PAHs.

Lastly, we investigated the possibility of ionic fragments (Ni<sup>+</sup>, Fe<sup>+</sup>) as precursors to the observed neutral metals. For these ions our fluorescence model suggests *g*-factors many orders of magnitude lower than the neutrals, and ionic fragments would need to neutralize via charge exchange or radiative/dielectronic capture within a distance of order  $\sim$ hundreds of kilometers to explain the observed spatial profiles. Capture of a free electron to produce neutral metal atoms is unlikely provided the low electron densities in the inner coma, cf.  $n_e \leq 10^3$  at 67P (Myllys et al. 2019).

Ion impact experiments of iron carbonyl (Indrajith et al. 2019) indicate Fe $^+$  energies post-fragmentation in the range of 0.1–1 eV (0.6–1.9 km s $^{-1}$ ). At these low energies the cross section for charge exchange is likely small,  $<10^{-17}$  cm $^2$  (see Friedman & DuCharme 2017 and references therein). For a nominal neutral density in the inner coma of  $10^{10}$  cm $^{-3}$ , the mean free path for charge exchange is on the order of  $10^4$  km, too large to explain the observed spatial profiles. Thus, we fully expect that the atomic iron and nickel are released into the coma as neutral products of photochemistry.

### 5.3. Sensitivity to Heliocentric Velocity

We computed fluorescence efficiencies of our observed Ni and Fe lines as a function of heliocentric velocity. Figure 10

shows the calculated fluorescence efficiencies for  $r_h = 1$  au for five observed lines of Ni I (top) and Fe I (bottom) as a function of heliocentric velocity; calculated fluorescence efficiencies for all of our observed metal lines are available in the Appendix.

Manfroid et al. (2021) noted that the metal fluorescence efficiencies are sensitive to heliocentric velocity, as the driving fluxes for many of the metal emission lines reside at or near absorption features in the solar spectrum. In Figure 10, as  $v_h$  changes, the spectral location of the driving flux sweeps over absorption features, resulting in g-factors that vary by a factor of  $\sim$ 3 over the range  $v_h = \pm 50 \text{ km s}^{-1}$ . These changes are comparable to the velocity sensitivity of molecular emission, e.g., a factor of 2 for the NH A-X (0–0) band in the range  $v_h = \pm 80 \text{ km s}^{-1}$  (Meier et al. 1998) and a factor of 4 for OH A-X (0–0) across  $v_h = \pm 60 \text{ km s}^{-1}$  (Schleicher & A'Hearn 1988). Lines of Fe I have smaller g-factors but exhibit greater sensitivity to heliocentric velocity, in some cases nearing a factor of 10 (Fe I 373.71 nm). For both metal atoms, velocity-sensitive g-factors are insensitive to the choice of line profile as either delta function or Doppler broadened.

In light of our previous discussion and the agreement between fluorescence models and observed line ratios, it is likely that the metal emission is purely fluorescent in origin. The observation of two lines, one strongly sensitive to  $v_h$  and one insensitive to  $v_h$ , from a single comet at multiple heliocentric velocities would allow for confirmation of a definitive fluorescence mechanism via comparison with computed g-factors. Two potential line ratios (Figure 10, bottom panel) for this purpose would be Ni I I(352.54)/I(347.25) or Fe I I(371.99)/I(373.71). Any line ratio involving Fe I 371.99 nm is favorable, as the line is among the strongest observed iron features (see the line list of Manfroid et al.  $2021^9$ ) and the g-factor exhibits a strong dependence on heliocentric velocity.

# 6. Summary

We developed a many-level fluorescence model compatible with atomic data in the NIST ASD (Kramida et al. 2020) and made the code publicly available. Using our fluorescence model, we searched archived data of the 1996 apparition of comet Hyakutake for possible metal lines identified in other comets by Manfroid et al. (2021) and Guzik & Drahus (2021). The nucleus-centered spectrum of C/1996 B2 (Hyakutake) was compared against synthetic fluorescence spectra of atomic metals and spectra from laboratory plasmas seeded with nickel and iron. We identified 14 emission lines of Ni I and 22 lines of Fe I in the comet spectrum. Agreement between fluorescence models and observed features of Ni I and Fe I was achieved within a factor of  $\sim\!\!2$  on average.

Assuming fluorescence emission, we derived column densities of nickel and iron atoms, from which we used the total number of particles within our aperture to inform Haser models to estimate the production rates  $Q_{\rm Ni} = (2.6-4.1)\times 10^{22}~{\rm s}^{-1}$  and  $Q_{\rm Fe} = (0.4-2.8)\times 10^{23}~{\rm s}^{-1}$ . Using our derived column densities to determine the Ni/Fe abundance ratio, we find  $\log_{10}[{\rm Ni/Fe}] = -0.15\pm 0.07$ , a value that differs significantly from abundances observed for the Sun, C/1965 S1 (Ikeya-Seki), and in situ measurements of dust in 1P/Halley. Our abundance ratios are in

<sup>&</sup>lt;sup>9</sup> Line list available as supplementary information at https://www.researchsquare.com/article/rs-101492/v1.

line with those observed in other solar system comets and 2I/Borisov.

We considered the possible sources and excitation mechanisms of the atomic iron and nickel. The observed spectrum is fully consistent with photofluorescence, with no evidence for the presence of highly excited states that could indicate a dissociative excitation process. We suggest that the strong dependence of the fluorescence efficiency on the heliocentric velocity can provide a direct test of this mechanism.

The distribution of the emission of Fe I and Ni I can be explained by the dissociation of a short-lived parent. Two possible parents have been proposed thus far: metal carbonyls, and PAH complexes bearing metal atoms. PAH abundances with respect to water are of similar magnitude to Ni/Fe (Klotz et al. 1996; Bodewits & Bromley 2021) and remain a possible precursor to atomic metals in the coma. Metal carbonyls, alternatively, are expected to sublimate at temperatures similar to CO ice and have the requisite characteristics to explain the observed Ni/Fe abundances. UV absorption cross sections of iron and nickel carbonyl suggest that these precursor molecules, if present, are fully stripped of CO groups to produce atomic nickel and iron within 120-150 km. UV absorption cross sections of the intermediate dissociation products are required to support or refute this possibility. The similarity in UV absorption cross sections for nickel/iron carbonyls suggests that the depletion of Ni/Fe with respect to solar is not driven by differences in the absorption properties but is imprinted during initial formation of the precursors.

The discoveries of Ni I and Fe I emission in comets have elucidated a new diagnostic to cometary scientists in which some information on the organometallic inventories of comets can be probed without waiting for rare sungrazer events or sample return missions. Given the propensity of nickel and iron emission in the UV–visible range, these lines may be analyzed

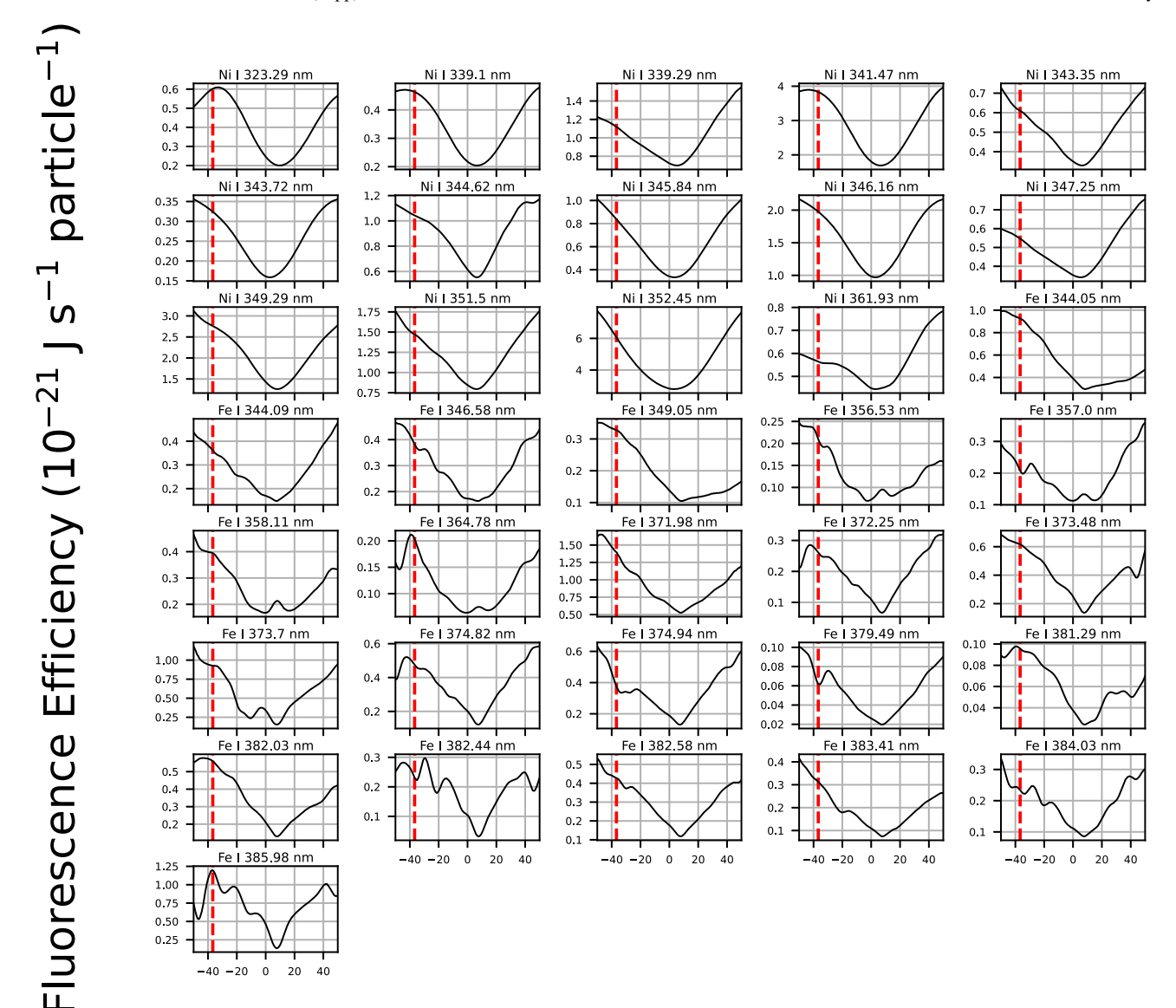
alongside typical molecular features. With sufficient sampling, these discoveries may shed light on aspects of as-yet-unexplored organic astrochemistry.

We thank John Noonan (Lunar and Planetary Lab, U. Arizona) for his helpful discussions during the development of the fluorescence model. Special thanks are extended to Neil Cole-Filipiak and Krupa Ramasesha of Sandia National Laboratories for engaging discussions of iron/nickel carbonyl photochemistry, and Damien Hutsemekers (University of Liège) for thoughtful comments on the fluorescence modeling. The authors gratefully acknowledge funding support from the National Science Foundation (grant Nos. 1815833, 1815932, and 1816984). The Compact Toroidal Hybrid measurements were supported by U.S. DOE grant No. DE-FG-02-00ER54610. We are grateful for the support of the Auburn University Hopper Cluster for their assistance and computing resources utilized for this work. We extend a special thank-you to the observing team (A'Hearn et al. 2015b) for collecting and archiving their data through the Planetary Data System, and the NIST ASD team for acquiring, compiling, and archiving useful

*Software:* Python3, NumPy (Harris et al. 2020), SciPy (Virtanen et al. 2020), Small Body Python (sbpy, Mommert et al. 2019).

# Appendix Fluorescence Efficiencies of Observed Metal Lines

Using the fluorescence model (see Section 3), we computed heliocentric-velocity-dependent g-factors for the observed nickel and iron emission features. Figure 11 shows the computed fluorescence efficiencies of all detected lines on a grid of heliocentric velocities spanning -50 to +50 km/s.



# Heliocentric Velocity (km/s)

Figure 11. Calculated fluorescence efficiencies for observed metal lines in Hyakutake as a function of heliocentric velocity. The velocity of Hyakutake  $(-36.7 \text{ km s}^{-1})$  is indicated by a vertical red line in each plot. Each spectrum is shown with independent linear intensity scale.

# **ORCID** iDs

S. J. Bromley https://orcid.org/0000-0003-2110-8152

S. D. Loch https://orcid.org/0000-0002-3822-6756

J. P. Marler https://orcid.org/0000-0002-1626-5615

J. Országh https://orcid.org/0000-0002-4309-6060

K. Venkataramani https://orcid.org/0000-0003-3321-1472

D. Bodewits https://orcid.org/0000-0002-2668-7248

# References

A'Hearn, M. F., Belton, M. J. S., Delamere, W. A., et al. 2011, Sci, 332, 1396
A'Hearn, M. F., Millis, R. C., Schleicher, D. G., Osip, D. J., & Birch, P. V. 1995, Icar, 118, 223

A'Hearn, M. F., Swamy, K. S. K., Wellnitz, D. D., & Meier, R. 2015a, AJ, 150, 5

A'Hearn, M. F., Wellnitz, D. D., & Meier, R. 2013, in IAU Symp. 297, The Diffuse Interstellar Bands (Cambridge: Cambridge Univ. Press), 216 A'Hearn, M. F., Wellnitz, D. D., & Meier, R. 2015b, Spectra of C/1996 B2 (Hyakutake) for Multiple Offsets from Photocenter, Planetary Data System, urn:nasa:pds:gbo-kpno:hyakutake\_spectra::1.0

Altwegg, K., Balsiger, H., & Fuselier, S. A. 2019, ARA&A, 57, 113

Berger, E. L., Zega, T. J., Keller, L. P., & Lauretta, D. S. 2011, GeCoA, 75, 3501

Bockelée-Morvan, D., & Biver, N. 2017, RSPTA, 375, 20160252

Bodewits, D., & Bromley, S. J. 2021, Natur, 593, 349

Bodewits, D., Orszagh, J., Noonan, J., Ďurian, M., & Matejčík, V. 2019, ApJ, 885, 167

Bromley, S. J., Johnson, C. A., Ennis, D. A., et al. 2020, ApJS, 250, 19 Brownlee, D. 2014, AREPS, 42, 179

Chance, K., & Kurucz, R. 2010, JOSRT, 111, 1289

Cochran, A. L., & Schleicher, D. G. 1993, Icar, 105, 235

Coddington, O. M., Richard, E. C., Harber, D., et al. 2021, GeoRL, 48, e91709 Cole-Filipiak, N. C., Troß, J., Schrader, P., McCaslin, L. M., & Ramasesha, K. 2021, JChPh, 154, 134308

Cremonese, G., Boehnhardt, H., Crovisier, J., et al. 1997, ApJL, 490, L199 Cremonese, G., Huebner, W., Rauer, H., & Boice, D. 2002, AdSpR, 29, 1187 Crismani, M. M. J., Schneider, N. M., Evans, J. S., et al. 2018, JGRE, 123, 2613

```
Distefano, G. 1970, JRNBA, 74A, 233
Feldman, P. D., Cochran, A. L., & Combi, M. R. 2004, in Comets II, ed.
   M. C. Festou, H. U. Keller, & H. A. Weaver (Tucson, AZ: Univ. Arizona
   Press), 425
Fernando, A. M., Bernath, P. F., Hodges, J. N., & Masseron, T. 2018, JQSRT,
   217, 29
Festou, M. C. 1981, A&A, 95, 69
Fioroni, M. 2014, PCCP, 16, 24312
Fontenla, J. M., Landi, E., Snow, M., & Woods, T. 2014, SoPh, 289, 515
Friedman, B., & DuCharme, G. 2017, JPhB, 50, 115202
Fuss, W., Schmid, W. E., & Trushin, S. A. 2001, JPCA, 105, 333
Gao, J., Bouwman, J., Berden, G., & Oomens, J. 2016, JPCA, 120, 7800
Guzik, P., & Drahus, M. 2021, Natur, 593, 375
Hall, L. A., & Anderson, G. P. 1991, JGR, 96, 12,927
Harris, C. R., Millman, K. J., van der Walt, S. J., et al. 2020, Natur, 585, 357
Hartwell, G., Knowlton, S., Hanson, J., Ennis, D., & Maurer, D. 2017, Fusion
      ence and Technology, 72, 76
Haser, L., Oset, S., & Bodewits, D. 2020, PSJ, 1, 83
Huebner, W., & Mukherjee, J. 2015, P&SS, 106, 11
Hutsemékers, D., Manfroid, J., Jehin, E., Opitom, C., & Moulane, Y. 2021,
    &A, 652, L1
Indrajith, S., Rousseau, P., Huber, B. A., et al. 2019, The Journal of Physical
   Chemistry C, 123, 10639
Jessberger, E. K., Christoforidis, A., & Kissel, J. 1988, Natur, 332, 691
Johnson, C. A., Ennis, D. A., Loch, S. D., et al. 2019, PPCF, 61, 095006
Jones, G. H., Knight, M. M., Battams, K., et al. 2017, SSRv, 214, 20
Kerkeni, B., Aquino, A. J. A., Berman, M. R., & Hase, W. L. 2019, MolPh,
   117, 1392
Kim, S. J., A'Hearn, M., Wellnitz, D., Meier, R., & Lee, Y. 2003, Icar,
   166, 157
```

Klotz, A., Marty, P., Boissel, P., et al. 1996, P&SS, 44, 957

111, 7687

Kotzian, M., Roesch, N., Schroeder, H., & Zerner, M. C. 1989, JAChS,

```
Kovačević, J., Popović, L. Č., & Dimitrijević, M. S. 2010, ApJS, 189, 15
Kramida, A., Yu. Ralchenko, R. J. & NIST ASD Team 2020, NIST Atomic
  Spectra Database (ver. 5.8) (Gaithersburg, MD: NIST), https://physics.nist.
Kurucz, R. L., Furenlid, I., Brault, J., & Testerman, L. 1984, Solar flux atlas
  from 296 to 1300 nm, National Solar Observatory Atlas (Sunspot, NM:
  National Solar Observatory)
Leadbeater, N. 1999, Coordination Chemistry Reviews, 188, 35
Manfroid, J., Hutsemékers, D., & Jehin, E. 2021, Natur, 593, 372
McKay, A. J., DiSanti, M. A., Kelley, M. S. P., et al. 2019, AJ, 158, 128
Meier, R., Wellnitz, D., Kim, S. J., & A'Hearn, M. F. 1998, Icar, 136, 268
Mommert, M. P., Kelley, M. S., de Val-Borro, M., et al. 2019, JOSS, 4,
Morton, D. C. 2000, ApJS, 130, 403
Myllys, M., Henri, P., Galand, M., et al. 2019, A&A, 630, A42
Nierenberg, A. M., Gilman, D., Treu, T., et al. 2019, MNRAS, 492,
Öberg, K. I., Guzmán, V. V., Merchantz, C. J., et al. 2017, ApJ, 839, 43
Pollack, J. B., Hollenbach, D., Beckwith, S., et al. 1994, ApJ, 421, 615
Preston, G. W. 1967, ApJ, 147, 718
Protopapa, S., Sunshine, J. M., Feaga, L. M., et al. 2014, Icar, 238, 191
Ribar, A., Danko, M., Országh, J., et al. 2015, EPJD, 69, 117
Roos-Serote, M., Barucci, A., Crovisier, J., et al. 1995, GeoRL, 22, 1621
Rubin, M., Altwegg, K., Balsiger, H., et al. 2019, MNRAS, 489, 594
Schleicher, D. G., & A'Hearn, M. F. 1988, ApJ, 331, 1058
Schleicher, D. G., & Osip, D. J. 2002, Icar, 159, 210
Slaughter, C. D. 1969, AJ, 74, 929
Strøm, P. A., Bodewits, D., Knight, M. M., et al. 2020, PASP, 132, 101001
Sunshine, J. M., & Feaga, L. M. 2021, PSJ, 2, 92
Villanueva, G., Smith, M., Protopapa, S., Faggi, S., & Mandell, A. 2018,
  JOSRT, 217, 86
Virtanen, P., Gommers, R., Oliphant, T. E., et al. 2020, NatMe, 17, 261
```

Wyckoff, S., Heyd, R. S., & Fox, R. 1999, ApJL, 512, L73